PROCEEDINGS A

rspa.royalsocietypublishing.org

Research

Article submitted to journal

Subject Areas:
mechanical engineering

Keywords:
electro-osmotic flow, electric double layer, rotating channel, Ekman layer, secondary flow

Author for correspondence:
Chiu-On Ng
e-mail: cong@hku.hk

Electro-osmotic flow in a rotating rectangular microchannel

Chiu-On Ng and Cheng Qi

Department of Mechanical Engineering, The University of Hong Kong, Pokfulam Road, Hong Kong

An analytical model is presented for low-Rossby-number electro-osmotic flow in a rectangular channel rotating about an axis perpendicular to its own. The flow is driven under the combined action of Coriolis, pressure, viscous and electric forces. Analytical solutions in the form of eigenfunction expansions are developed for the problem, which is controlled by the rotation parameter (or the inverse Ekman number), the Debye parameter, the aspect ratio of the channel, and the distribution of zeta potentials on the channel walls. Under the conditions of fast rotation and a thin electric double layer (EDL), an Ekman–EDL layer develops on the horizontal walls. This is essentially an Ekman layer subjected to electrokinetic effects. The flow structure of this boundary layer as a function of the Ekman layer thickness normalised by the Debye length is investigated in detail in this study. It is also shown that the channel rotation may have qualitatively different effects on the flow rate, depending on the channel width and the zeta potential distributions. Axial and secondary flows are examined in detail to reveal how the development of a geostrophic core may lead to a rise or fall of the mean flow.

THE ROYAL SOCIETY PUBLISHING

1. Introduction

Electro-osmotic (EO) pumping is one of the major mechanisms used to control or drive fluid flow in a microchannel. This method draws upon an unbalanced charge distribution in the electric double layer (EDL) that develops on a fluid–solid interface. Many substances (e.g. glass) will acquire a surface electric charge when brought in contact with an electrolyte solution. Ions of opposite charge, or counterions, will be attracted to the surface, while ions of the same charge, or coions, are repelled from the surface. Near the charged surface forms a two-layer structure: an inner layer of immobile ions, also called the Stern layer, and an outer diffuse layer containing more counterions than coions so as to neutralise the surface charge. The electric potential on the interface between the Stern and diffuse layers is known as the zeta potential, which determines the ionic strength of the EDL. When under an applied electric potential, the free ions together with the fluid in the EDL will move. Through the action of viscosity, the bulk fluid will be pulled into motion as well, resulting in the so-called electro-osmotic flow (EOF). Compared with pressure-driven flow, EOF may offer a more precise flow control, a flatter velocity profile (thereby less hydrodynamic dispersion), and a flow rate that is less dependent on the channel size. EOF is especially suitable when a small sample is processed.

While EOF has been extensively studied in the literature, EOF in a rotating environment did not receive attention until recently. Motivated by Duffy *et al.* [1], Chang & Wang [2] pioneered a theoretical study on rotating EOF over an infinite plate or in a channel bounded by two parallel plates. Based on the Debye–Hückel approximation, analytical solutions were developed for the axial and transverse flows as functions of the parameters characterising the rotation, viscous transport and electrokinetics. In their two-plate problem, Chang & Wang [2] found that the transverse flow rate is the maximum when the rotation number is of order unity. As the rotation number tends to infinity, both the axial and transverse flow rates will diminish to zero. The work by Chang & Wang was recently extended by Xie & Jian [3] and Li *et al.* [4] for rotating EOF of non-Newtonian fluids in a slit channel.

An area where rotating EOF may find great potential use is centrifugal microfluidics. The so-called compact disc-based fluidics is a system in which fluid is pumped simply by centrifugal force that is generated as the disk spins. The system is highly portable, and allows a large number of chemical assays to be conducted in parallel under identical conditions; see, among many others, Duffy *et al.* [1] and Gorkin *et al.* [5]. A centrifugal microfluidic system may be easy to operate, but often times lacks flexibility. The only control is the spinning speed, and the rest is left to a complicated circuitry involving hydrophobic burst valves to be hard-wired on a compact disc (CD). To enhance flow control and separation efficiency, some researchers have proposed to complement centrifugal pumping with electrokinetic pumping. A dual-pumping CD-like microfluidic system has been put forward by Wang *et al.* [6] for biomedical separation. They developed a multi-channel electrophoretic separation CD system that worked under the interaction between the centrifugal and electric forces. They found that, through the adjustment of the applied electric field, a higher separation efficiency could be achieved by centrifugation. They also remarked that their separation system could have the advantages of lower joule-heat generation, low chemistry reaction, and little variation of the ion concentration during processes. Further works on electrophoresis on a rotating platform have been reported by Boettcher *et al.* [7] and Martinez-Duarte *et al.* [8]. Soong & Wang [9] also presented a model for rotation driven electrokinetic flow in a micro-gap between two rotating disks. There also exists a sizable body of literature on electrohydrodynamic instability of rotating fluids [10–13].

EOF in a rotating channel is a problem of fundamental interest as it involves the balance between the Coriolis force, pressure gradient, viscous force and electric body force. Taking into account all these effects, the present study aims to develop a theoretical model for EOF in a rectangular channel rotating about an axis perpendicular to its own. Our model is broader in scope than that by Chang & Wang [2] in the following aspects. First, Chang & Wang [2] have simplified their model by ignoring lateral confinement in their two-plate problem. We here

consider a channel with side walls, and as a result the net mass flux in the transverse direction is always zero. The need to consider a channel of finite width stems from the fact that rotating microchannels are usually fabricated with a rectangular or circular cross section (e.g. Duffy *et al.* [1]; Ducrée *et al.* [14]). We shall show that our model is fundamentally different from that of Chang & Wang [2] even in the limit of a very wide channel. Also, owing to the absence of lateral confinement, the secondary flow field in their problem can only be one dimensional, while that in ours is two dimensional in the form of circulatory roll cells. Second, the transverse pressure gradient, which is omitted in their problem, is accounted for in this study. This term will be shown to play a very important role in controlling not only the axial flow but also the secondary flow. Third, with side walls, we may consider EOFs due to different configurations of the wall potential distributions. We shall show that when only the horizontal walls are charged, the effect of rotation on the flow can be dramatically different than that when all the walls are charged.

This paper is organised as follows. In §2, the mathematical formulation of our problem is presented. We shall consider a regime where the inertia effects are negligible, and the rotation parameter (or the inverse Ekman number) is of order unity or larger. To focus on the effects due to electrokinetics, the primary flow is driven solely by an applied electric field. On adopting the Debye–Hückel approximation, an analytical expression is deduced for the electric potential distribution in a rectangular channel with possibly different zeta potentials on the horizontal and vertical walls. The present problem is characterised by the ratios of the following dimensions to the channel height: the channel width, the Ekman layer thickness, and the Debye length (or the EDL layer thickness). In §3, analytical solutions to the problem are developed. The solutions for the three velocity components and the pressure are found in the form of eigenfunction expansions. In §4, some limiting cases are investigated. In particular, for a very wide channel, the problem simplifies to the one considered by Chang & Wang [2] but with an added term due to the transverse pressure gradient, which is required in order to balance the mass flux in the transverse direction. The introduction of the transverse pressure gradient makes the axial and transverse flows different from those deduced by Chang & Wang [2]. In the limit of large rotation and Debye parameters, the flow structure of an Ekman–EDL layer is deduced in §4(c). The Ekman–EDL layer is a boundary layer incorporating the effects due to Coriolis, viscous and electric forces. It is characterised by the dimensionless Debye parameter that is normalized by the Ekman layer thickness. In §5, the axial and secondary flows in a rotating channel of a finite aspect ratio are examined. It is found that these flows may change in different manners with the rotation and Debye parameters, depending on the channel width and the distribution of zeta potentials on the four walls. We shall formally show that as the rotation parameter becomes very large, the flow in the interior will tend to be geostrophic, thereby satisfying the Taylor–Proudman theorem, in the leading order. On attaining a geostrophic core, the axial flow in the interior may increase as the rotation parameter increases if only the horizontal walls are charged. This leads to the possibility of a rotation-enhanced flow, which is in sharp contrast to what has been commonly known: rotation will reduce the rate of flow in a rotating channel. We here provide examples to demonstrate to the contrary.

2. Problem formulation

As is shown in figure 1, the present problem is to consider electro-osmotic (EO) flow of a Newtonian fluid through a rotating rectangular microchannel of height $2h$ and width $2b$. Flow description is made with respect to a right-handed coordinate system (x, y, z) that rotates with the channel: the x-axis is along the longitudinal centerline of the channel, while the y- and z-axes point along the transverse and vertical directions, respectively; see figure 1. An electric field E is applied purely along the x-direction, while the channel rotates about the z-axis at a constant rotational speed Ω.

The flow is incompressible and steady relative to the rotating frame. A microchannel being considered, the Reynolds number of the flow through the channel is typically very small, by which we may ignore the convective acceleration of the relative velocity. This amounts to placing

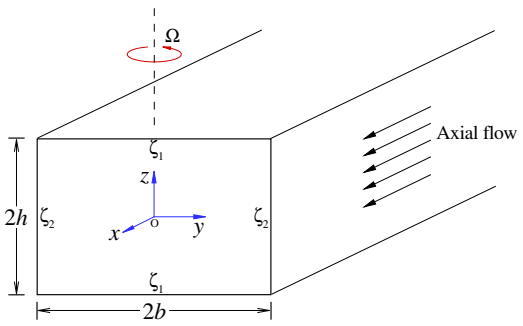

Figure 1. Definition sketch of the problem: electro-osmotic flow through a rotating rectangular channel of height $2h$ and width $2b$, with a zeta potential ζ_1 on the horizontal walls, and ζ_2 on the vertical walls.

the present problem in the regime of a very small Rossby number. Also ignoring gravity, the governing equations in the rotating frame (e.g. Greenspan [15]; Pedlosky [16]) are

$$\nabla \cdot \vec{u} = 0, \tag{2.1}$$

$$2\rho\vec{\Omega} \times \vec{u} = -\nabla p + \mu\nabla^2\vec{u} + \rho_e\vec{E}. \tag{2.2}$$

In these equations, $\vec{u} = (u, v, w)$ is the velocity seen in the rotating frame, $\vec{\Omega} = (0, 0, \Omega)$, $\vec{E} = (E, 0, 0)$, ρ is the fluid density, μ is the dynamic viscosity of the fluid, ρ_e is the free charge density in the electric double layer (EDL) formed near the channel walls, and p is the reduced pressure (i.e. the pressure subtracting the centrifugal pressure).

Flow is assumed to be fully-developed so that it is independent of the axial coordinate x. Primary EOF of velocity $u(y, z)$ is driven by the Lorentz force, the last term on the right side of (2.2). Secondary flow of velocity components $v(y, z)$, $w(y, z)$ arises owing to the Coriolis acceleration, the term on the left side of (2.2). As the Coriolis force is always perpendicular to the associated velocity, the secondary flow will affect the primary flow, and vice versa. We further assume that there is no net pressure gradient to drive the primary flow. Pressure gradient is, however, induced internally to maintain the secondary flow in the cross-sectional (y, z)-plane.

An EDL is formed near each of the four walls when these walls are charged. The electric potential $\psi(y, z)$ in the EDL is related to the charge density ρ_e by the Poisson equation

$$\nabla^2\psi = -\frac{\rho_e}{\epsilon}, \tag{2.3}$$

where ϵ is the dielectric permittivity of the liquid electrolyte. We here consider a symmetrical electrolyte of valence Z and assume a Boltzmann distribution of the electrolyte ions in the EDL. The charge density is then given by

$$\rho_e = -2Zen_\infty \sinh\left(\frac{Ze\psi}{k_BT}\right), \tag{2.4}$$

where e is the fundamental charge, n_∞ is the bulk concentration, k_B is Boltzmann's constant, and T is the absolute temperature. Putting (2.4) into (2.3) will form the well-known Poisson–Boltzmann equation. For very small potentials, $|Ze\psi/k_BT| \ll 1$, the Poisson–Boltzmann equation can be linearised to

$$\nabla^2\psi = \kappa^2\psi, \tag{2.5}$$

where $\kappa = (2Z^2e^2n_\infty/\epsilon k_BT)^{1/2}$ is called the Debye parameter, the inverse of which is the Debye shielding length of the EDL. The linearisation of the Poisson–Boltzmann equation is also known as the Debye–Hückel approximation.

To allow some generality, we assume that the walls may have different wall (or zeta) potentials. On the top and bottom walls

$$\psi(y, \pm h) = \zeta_1, \tag{2.6}$$

while on the left and right side walls

$$\psi(\pm b, z) = \zeta_2. \tag{2.7}$$

To satisfy the condition for the Debye–Hückel approximation, these wall potentials should be much smaller in magnitude than the thermal potential $k_B T/Ze$, which has the value of 25 mV at room temperature for a binary electrolyte. The solution to (2.5) satisfying the boundary conditions (2.6) and (2.7) is readily found by eigenfunction expansion:

$$\psi(y, z) = \zeta_1 \frac{\cosh(\kappa z)}{\cosh(\kappa h)} + 2 \sum_{n=1}^{\infty} \frac{(-1)^{n+1}}{\alpha_n h} \left[\zeta_2 - \frac{\alpha_n^2}{\beta_n^2} \zeta_1\right] \frac{\cosh(\beta_n y)}{\cosh(\beta_n b)} \cos(\alpha_n z), \tag{2.8}$$

where

$$\alpha_n = (2n-1)\,\frac{\pi}{2h}, \qquad \beta_n = \left(\alpha_n^2 + \kappa^2\right)^{1/2}. \tag{2.9}$$

Let us introduce the following normalized variables or parameters, which are distinguished by overhead carets:

$$\left.\begin{aligned} \left(\hat{x},\, \hat{y},\, \hat{z},\, \hat{b}\right) &= (x,\, y,\, z,\, b)\,/h, \qquad \left(\hat{\kappa},\, \hat{\alpha}_n,\, \hat{\beta}_n\right) = (\kappa,\, \alpha_n,\, \beta_n)\, h, \\ (\hat{u},\, \hat{v},\, \hat{w}) &= (u,\, v,\, w)\,/U, \quad \left(\hat{\psi},\, \hat{\zeta}_1,\, \hat{\zeta}_2\right) = (\psi,\, \zeta_1,\, \zeta_2)\,/\tilde{\zeta}, \quad \hat{p} = p/(\mu U/h) \end{aligned}\right\} \tag{2.10}$$

where $\tilde{\zeta}$ is a characteristic scale for the zeta potential (which can be ζ_1 or ζ_2, depending on the problem), and U is the Helmholtz–Smoluchowski velocity given by

$$U = -\epsilon \tilde{\zeta} E/\mu. \tag{2.11}$$

In terms of these normalized variables, the governing equations have the following non-dimensional component form:

$$-\omega \hat{v} = \frac{\partial^2 \hat{u}}{\partial \hat{y}^2} + \frac{\partial^2 \hat{u}}{\partial \hat{z}^2} + \hat{\kappa}^2 \hat{\psi}, \tag{2.12}$$

$$\omega \hat{u} = -\frac{\partial \hat{p}}{\partial \hat{y}} + \frac{\partial^2 \hat{v}}{\partial \hat{y}^2} + \frac{\partial^2 \hat{v}}{\partial \hat{z}^2}, \tag{2.13}$$

$$0 = -\frac{\partial \hat{p}}{\partial \hat{z}} + \frac{\partial^2 \hat{w}}{\partial \hat{y}^2} + \frac{\partial^2 \hat{w}}{\partial \hat{z}^2}, \tag{2.14}$$

$$\frac{\partial \hat{v}}{\partial \hat{y}} + \frac{\partial \hat{w}}{\partial \hat{z}} = 0, \tag{2.15}$$

where

$$\omega = 2\rho \Omega h^2/\mu \tag{2.16}$$

is the dimensionless rotation parameter, also known as the inverse Ekman number, and

$$\hat{\psi}(\hat{y}, \hat{z}) = \hat{\zeta}_1 \frac{\cosh(\hat{\kappa}\hat{z})}{\cosh(\hat{\kappa})} + \sum_{n=1}^{\infty} \hat{\psi}_n \frac{\cosh(\hat{\beta}_n \hat{y})}{\cosh(\hat{\beta}_n \hat{b})} \cos(\hat{\alpha}_n \hat{z}), \tag{2.17}$$

in which

$$\hat{\psi}_n = 2 \frac{(-1)^{n+1}}{\hat{\alpha}_n} \left[\hat{\zeta}_2 - \frac{\hat{\alpha}_n^2}{\hat{\beta}_n^2} \hat{\zeta}_1\right], \qquad \hat{\alpha}_n = (2n-1)\,\frac{\pi}{2}, \qquad \hat{\beta}_n = \left(\hat{\alpha}_n^2 + \hat{\kappa}^2\right)^{1/2}. \tag{2.18}$$

Note that the rotation parameter can be written as follows:

$$\omega = 2 \left(\frac{h}{\delta_E}\right)^2, \tag{2.19}$$

where δ_E is the Ekman layer thickness given by

$$\delta_E = \left(\frac{\nu}{\Omega}\right)^{1/2}, \tag{2.20}$$

in which $\nu = \mu/\rho$ is the kinematic viscosity. Depending on the design, the rotational speed of a centrifuge can be $O(10^3)$ rpm or faster, which for a liquid of $\nu \sim 10^{-6}$ m^2/s will give an Ekman layer thickness $\delta_E \sim 100$ μm or thinner. As the cross-sectional dimension of a rotating microchannel can vary over a wide range of $O(1-10^3)$ μm [1], it is reasonable for us to consider the rotation parameter ω to be as large as $O(100)$, which is consistent with what has been estimated by Chang & Wang [2]. The other parameter of importance is the normalized Debye parameter $\hat{\kappa} = \kappa h$. It is well known that the EDL thickness is $\kappa^{-1} \sim 10$ nm or thicker, depending on the ion concentration. Hence, we should in principle take $\hat{\kappa} \geq O(10)$. However, in order to see theoretical trends, we may also consider $\hat{\kappa} = O(1)$.

Assuming that the walls are non-slipping, the flow is to satisfy the no-slip condition on the boundaries:

$$\hat{u} = \hat{v} = \hat{w} = 0 \qquad \text{at} \quad \hat{y} = \pm\hat{b} \quad \text{and} \quad \hat{z} = \pm 1. \tag{2.21}$$

Equations (2.12)–(2.15) will be solved for $\hat{u}$, $\hat{v}$, $\hat{w}$ and $\hat{p}$ in the following section. The forcing and the boundary conditions dictate that $\hat{u}$ and $\hat{v}$ are even functions of $\hat{y}$ and $\hat{z}$. It follows that $\hat{w}$ is an odd function of $\hat{y}$ and $\hat{z}$. Unless stated otherwise, normalized variables will be used in the following analysis. Also, for simplicity, we shall drop the overhead carets from these dimensionless quantities from here onward.

3. Solution to the problem

(a) Particular solution

The forcing term being the last term on the right side of (2.12), the particular solution to the inhomogeneous problem can be found straightforwardly as follows:

$$u_p(y,z) = -\frac{\kappa^4\zeta_1}{\kappa^4+\omega^2}\frac{\cosh(\kappa z)}{\cosh(\kappa)} + \sum_{n=1}^{\infty} U_n \frac{\cosh(\beta_n y)}{\cosh(\beta_n b)}\cos(\alpha_n z), \tag{3.1}$$

$$v_p(y,z) = -\frac{\omega\kappa^2\zeta_1}{\kappa^4+\omega^2}\frac{\cosh(\kappa z)}{\cosh(\kappa)} + \sum_{n=1}^{\infty} V_n \frac{\cosh(\beta_n y)}{\cosh(\beta_n b)}\cos(\alpha_n z), \tag{3.2}$$

$$w_p(y,z) = \sum_{n=1}^{\infty} W_n \frac{\sinh(\beta_n y)}{\cosh(\beta_n b)}\sin(\alpha_n z), \tag{3.3}$$

$$p_p(y,z) = \sum_{n=1}^{\infty} P_n \frac{\sinh(\beta_n y)}{\cosh(\beta_n b)}\cos(\alpha_n z), \tag{3.4}$$

where

$$U_n = -\frac{\kappa^6}{\kappa^6 - \omega^2\alpha_n^2}\psi_n, \tag{3.5}$$

$$V_n = \frac{\omega\alpha_n^2\kappa^2}{\kappa^6 - \omega^2\alpha_n^2}\psi_n, \tag{3.6}$$

$$W_n = -\frac{\omega\alpha_n\beta_n\kappa^2}{\kappa^6 - \omega^2\alpha_n^2}\psi_n, \tag{3.7}$$

$$P_n = \frac{\omega\beta_n\kappa^4}{\kappa^6 - \omega^2\alpha_n^2}\psi_n, \tag{3.8}$$

and

$$\psi_n = 2\frac{(-1)^{n+1}}{\alpha_n}\left[\zeta_2 - \frac{\alpha_n^2}{\beta_n^2}\zeta_1\right], \qquad \alpha_n = (2n-1)\,\frac{\pi}{2}, \qquad \beta_n = \left(\alpha_n^2 + \kappa^2\right)^{1/2}. \tag{3.9}$$

(b) Complementary solution

By virtue of the fact the axial flow is symmetrical about both the y- and z-axes, the general solution to the homogeneous problem can be written in the following form

$$u_c(y,z) = \sum_{n=1}^{\infty} U_{1n}(y)\cos(\alpha_n z) + \sum_{n=1}^{\infty} U_{2n}(z)\cos(\gamma_n y), \tag{3.10}$$

$$v_c(y,z) = \sum_{n=1}^{\infty} V_{1n}(y)\cos(\alpha_n z) + \sum_{n=1}^{\infty} V_{2n}(z)\cos(\gamma_n y), \tag{3.11}$$

$$w_c(y,z) = \sum_{n=1}^{\infty} W_{1n}(y)\sin(\alpha_n z) + \sum_{n=1}^{\infty} W_{2n}(z)\sin(\gamma_n y), \tag{3.12}$$

$$p_c(y,z) = \sum_{n=1}^{\infty} P_{1n}(y)\cos(\alpha_n z) + \sum_{n=1}^{\infty} P_{2n}(z)\sin(\gamma_n y), \tag{3.13}$$

where

$$\gamma_n = (2n-1)\,\frac{\pi}{2b}. \tag{3.14}$$

On substituting these solutions into (2.12)–(2.15) without the forcing term, we obtain after some algebra the following two sets of equations.

For the first part of the complementary solution:

$$U_{1n}^{(6)} - 3\alpha_n^2 U_{1n}^{(4)} + 3\alpha_n^4 U_{1n}'' - \left(\alpha_n^6 + \omega^2\alpha_n^2\right) U_{1n} = 0, \tag{3.15}$$

$$V_{1n} = \omega^{-1}\left(-U_{1n}'' + \alpha_n^2 U_{1n}\right), \tag{3.16}$$

$$W_{1n} = -\alpha_n^{-1} V_{1n}', \tag{3.17}$$

$$P_{1n} = -\alpha_n^{-1}\left(W_{1n}'' - \alpha_n^2 W_{1n}\right). \tag{3.18}$$

For the second part of the complementary solution:

$$U_{2n}^{(6)} - 3\gamma_n^2 U_{2n}^{(4)} + \left(3\gamma_n^4 + \omega^2\right) U_{2n}'' - \gamma_n^6 U_{2n} = 0, \tag{3.19}$$

$$V_{2n} = \omega^{-1}\left(-U_{2n}'' + \gamma_n^2 U_{2n}\right), \tag{3.20}$$

$$W_{2n} = \gamma_n^{-3}\left(\omega U_{2n}' - V_{2n}''' + 2\gamma_n^2 V_{2n}'\right), \tag{3.21}$$

$$P_{2n} = \gamma_n^{-1}\left(-\omega U_{2n} + V_{2n}'' - \gamma_n^2 V_{2n}\right). \tag{3.22}$$

(i) To determine $U_{1n}, V_{1n}, W_{1n}, P_{1n}$

On letting $U_{1n} = \exp(\lambda y)$, we get from (3.15) the following characteristic equation

$$\lambda^6 - 3\alpha_n^2\lambda^4 + 3\alpha_n^4\lambda^2 - \alpha_n^6 - \omega^2\alpha_n^2 = 0. \tag{3.23}$$

This equation can be solved readily, giving the following six roots

$$\lambda = \pm\lambda_{1n} \qquad \text{or} \qquad \lambda = \pm\sigma_{1n} \pm \mathrm{i}\xi_{1n}, \tag{3.24}$$

where i is the complex unit, and

$$\lambda_{1n} = \left[\alpha_n^2 + (\omega\alpha_n)^{2/3}\right]^{1/2}, \tag{3.25}$$

$$\sigma_{1n} = \left[\frac{1}{2}\left(f_{1n} + \sqrt{f_{1n}^2 + g_{1n}^2}\right)\right]^{1/2}, \qquad \xi_{1n} = \frac{g_{1n}}{2\sigma_{1n}}, \tag{3.26}$$

in which

$$f_{1n} = \alpha_n^2 - \frac{1}{2}(\omega\alpha_n)^{2/3}, \qquad g_{1n} = \frac{\sqrt{3}}{2}(\omega\alpha_n)^{2/3}. \tag{3.27}$$

By symmetry about $y = 0$, U_{1n} is an even function of y. Hence, its general solution is expressible by

$$U_{1n}(y) = C_{1n}\frac{\cosh(\lambda_{1n}y)}{\cosh(\lambda_{1n}b)} + C_{2n}\frac{\cosh(\sigma_{1n}y)}{\cosh(\sigma_{1n}b)}\cos(\xi_{1n}y) + C_{3n}\frac{\sinh(\sigma_{1n}y)}{\sinh(\sigma_{1n}b)}\sin(\xi_{1n}y), \tag{3.28}$$

where C_{1n}, C_{2n}, C_{3n} are undetermined coefficients. From (3.16)–(3.18), we further get

$$\begin{aligned} V_{1n}(y) \;=\; & C_{1n}F_{1n}\frac{\cosh(\lambda_{1n}y)}{\cosh(\lambda_{1n}b)} \\ & + C_{2n}\left[F_{2n}\frac{\cosh(\sigma_{1n}y)}{\cosh(\sigma_{1n}b)}\cos(\xi_{1n}y) + F_{3n}\frac{\sinh(\sigma_{1n}y)}{\cosh(\sigma_{1n}b)}\sin(\xi_{1n}y)\right] \\ & + C_{3n}\left[F_{2n}\frac{\sinh(\sigma_{1n}y)}{\sinh(\sigma_{1n}b)}\sin(\xi_{1n}y) - F_{3n}\frac{\cosh(\sigma_{1n}y)}{\sinh(\sigma_{1n}b)}\cos(\xi_{1n}y)\right], \end{aligned} \tag{3.29}$$

$$\begin{aligned} W_{1n}(y) \;=\; & C_{1n}G_{1n}\frac{\sinh(\lambda_{1n}y)}{\cosh(\lambda_{1n}b)} \\ & + C_{2n}\left[G_{2n}\frac{\sinh(\sigma_{1n}y)}{\cosh(\sigma_{1n}b)}\cos(\xi_{1n}y) + G_{3n}\frac{\cosh(\sigma_{1n}y)}{\cosh(\sigma_{1n}b)}\sin(\xi_{1n}y)\right] \\ & + C_{3n}\left[G_{2n}\frac{\cosh(\sigma_{1n}y)}{\sinh(\sigma_{1n}b)}\sin(\xi_{1n}y) - G_{3n}\frac{\sinh(\sigma_{1n}y)}{\sinh(\sigma_{1n}b)}\cos(\xi_{1n}y)\right], \end{aligned} \tag{3.30}$$

$$\begin{aligned} P_{1n}(y) \;=\; & C_{1n}\Pi_{1n}\frac{\sinh(\lambda_{1n}y)}{\cosh(\lambda_{1n}b)} \\ & + C_{2n}\left[\Pi_{2n}\frac{\sinh(\sigma_{1n}y)}{\cosh(\sigma_{1n}b)}\cos(\xi_{1n}y) + \Pi_{3n}\frac{\cosh(\sigma_{1n}y)}{\cosh(\sigma_{1n}b)}\sin(\xi_{1n}y)\right] \\ & + C_{3n}\left[\Pi_{2n}\frac{\cosh(\sigma_{1n}y)}{\sinh(\sigma_{1n}b)}\sin(\xi_{1n}y) - \Pi_{3n}\frac{\sinh(\sigma_{1n}y)}{\sinh(\sigma_{1n}b)}\cos(\xi_{1n}y)\right], \end{aligned} \tag{3.31}$$

where

$$F_{1n} = \left(\alpha_n^2 - \lambda_{1n}^2\right)/\omega, \quad F_{2n} = \left(\alpha_n^2 - \sigma_{1n}^2 + \xi_{1n}^2\right)/\omega, \quad F_{3n} = 2\sigma_{1n}\xi_{1n}/\omega, \tag{3.32}$$

$$\left.\begin{aligned} G_{1n} = -\lambda_{1n}F_{1n}/\alpha_n, \qquad G_{2n} = -\left(\sigma_{1n}F_{2n} + \xi_{1n}F_{3n}\right)/\alpha_n, \\ G_{3n} = \left(\xi_{1n}F_{2n} - \sigma_{1n}F_{3n}\right)/\alpha_n, \end{aligned}\right\} \tag{3.33}$$

$$\left.\begin{aligned} \Pi_{1n} = -\omega\lambda_{1n}F_{1n}^2/\alpha_n^2, \qquad \Pi_{2n} = -\omega\left[\sigma_{1n}\left(F_{2n}^2 - F_{3n}^2\right) + 2\xi_{1n}F_{2n}F_{3n}\right]/\alpha_n^2, \\ \Pi_{3n} = \omega\left[\xi_{1n}\left(F_{2n}^2 - F_{3n}^2\right) - 2\sigma_{1n}F_{2n}F_{3n}\right]/\alpha_n^2. \end{aligned}\right\} \tag{3.34}$$

(ii) To determine U_{2n}, V_{2n}, W_{2n}, P_{2n}

On letting $U_{2n} = \exp(\lambda z)$, we get from (3.19) the following characteristic equation

$$\lambda^6 - 3\gamma_n^2\lambda^4 + \left(3\gamma_n^4 + \omega^2\right)\lambda^2 - \gamma_n^6 = 0. \tag{3.35}$$

After some algebra, the six roots of this equation can be found as follows:

$$\lambda = \pm\lambda_{2n} \qquad \text{or} \qquad \lambda = \pm\sigma_{2n} \pm \mathrm{i}\xi_{2n}, \tag{3.36}$$

where i is the complex unit, and

$$\lambda_{2n} = \left[\gamma_n^2 + S_n + T_n\right]^{1/2}, \tag{3.37}$$

$$\sigma_{2n} = \left[\frac{1}{2}\left(f_{2n} + \sqrt{f_{2n}^2 + g_{2n}^2}\right)\right]^{1/2}, \qquad \xi_{2n} = \frac{g_{2n}}{2\sigma_{2n}}, \tag{3.38}$$

in which

$$f_{2n} = \gamma_n^2 - \frac{1}{2}\left(S_n + T_n\right), \qquad g_{2n} = \frac{\sqrt{3}}{2}\left(S_n - T_n\right), \tag{3.39}$$

$$S_n = \left[-\frac{\omega^2\gamma_n^2}{2} + \sqrt{\left(\frac{\omega^2}{3}\right)^3 + \left(\frac{\omega^2\gamma_n^2}{2}\right)^2}\right]^{1/3}, \tag{3.40}$$

$$T_n = -\left[\frac{\omega^2\gamma_n^2}{2} + \sqrt{\left(\frac{\omega^2}{3}\right)^3 + \left(\frac{\omega^2\gamma_n^2}{2}\right)^2}\right]^{1/3}. \tag{3.41}$$

Note that $\gamma_n^2 + S_n + T_n$ is always positive, so λ_{2n} is always a real quantity.

By symmetry about $z = 0$, U_{2n} is an even function of z. Hence, its general solution is expressible by

$$U_{2n}(z) = C_{4n}\frac{\cosh(\lambda_{2n}z)}{\cosh(\lambda_{2n})} + C_{5n}\frac{\cosh(\sigma_{2n}z)}{\cosh(\sigma_{2n})}\cos(\xi_{2n}z) + C_{6n}\frac{\sinh(\sigma_{2n}z)}{\sinh(\sigma_{2n})}\sin(\xi_{2n}z), \tag{3.42}$$

where C_{4n}, C_{5n}, C_{6n} are undetermined coefficients. From (3.20)–(3.22), we further get

$$\begin{aligned} V_{2n}(z) \;=\; & C_{4n}H_{1n}\frac{\cosh(\lambda_{2n}z)}{\cosh(\lambda_{2n})} \\ & + C_{5n}\left[H_{2n}\frac{\cosh(\sigma_{2n}z)}{\cosh(\sigma_{2n})}\cos(\xi_{2n}z) + H_{3n}\frac{\sinh(\sigma_{2n}z)}{\cosh(\sigma_{2n})}\sin(\xi_{2n}z)\right] \\ & + C_{6n}\left[H_{2n}\frac{\sinh(\sigma_{2n}z)}{\sinh(\sigma_{2n})}\sin(\xi_{2n}z) - H_{3n}\frac{\cosh(\sigma_{2n}z)}{\sinh(\sigma_{2n})}\cos(\xi_{2n}z)\right], \end{aligned} \tag{3.43}$$

$$\begin{aligned} W_{2n}(z) \;=\; & C_{4n}I_{1n}\frac{\sinh(\lambda_{2n}z)}{\cosh(\lambda_{2n})} \\ & + C_{5n}\left[I_{2n}\frac{\sinh(\sigma_{2n}z)}{\cosh(\sigma_{2n})}\cos(\xi_{2n}z) + I_{3n}\frac{\cosh(\sigma_{2n}z)}{\cosh(\sigma_{2n})}\sin(\xi_{2n}z)\right] \\ & + C_{6n}\left[I_{2n}\frac{\cosh(\sigma_{2n}z)}{\sinh(\sigma_{2n})}\sin(\xi_{2n}z) - I_{3n}\frac{\sinh(\sigma_{2n}z)}{\sinh(\sigma_{2n})}\cos(\xi_{2n}z)\right], \end{aligned} \tag{3.44}$$

$$\begin{aligned} P_{2n}(z) \;=\; & C_{4n}\Upsilon_{1n}\frac{\cosh(\lambda_{2n}z)}{\cosh(\lambda_{2n})} \\ & + C_{5n}\left[\Upsilon_{2n}\frac{\cosh(\sigma_{2n}z)}{\cosh(\sigma_{2n})}\cos(\xi_{2n}z) + \Upsilon_{3n}\frac{\sinh(\sigma_{2n}z)}{\cosh(\sigma_{2n})}\sin(\xi_{2n}z)\right] \\ & + C_{6n}\left[\Upsilon_{2n}\frac{\sinh(\sigma_{2n}z)}{\sinh(\sigma_{2n})}\sin(\xi_{2n}z) - \Upsilon_{3n}\frac{\cosh(\sigma_{2n}z)}{\sinh(\sigma_{2n})}\cos(\xi_{2n}z)\right], \end{aligned} \tag{3.45}$$

where

$$H_{1n} = \left(\gamma_n^2 - \lambda_{2n}^2\right)/\omega, \quad H_{2n} = \left(\gamma_n^2 - \sigma_{2n}^2 + \xi_{2n}^2\right)/\omega, \quad H_{3n} = 2\sigma_{2n}\xi_{2n}/\omega, \tag{3.46}$$

$$\left.\begin{aligned} I_{1n} = \gamma_n H_{1n}/\lambda_{2n}, \qquad I_{2n} = \gamma_n\left(\sigma_{2n}H_{2n} - \xi_{2n}H_{3n}\right)/\left(\sigma_{2n}^2 + \xi_{2n}^2\right), \\ I_{3n} = \gamma_n\left(\xi_{2n}H_{2n} + \sigma_{2n}H_{3n}\right)/\left(\sigma_{2n}^2 + \xi_{2n}^2\right), \end{aligned}\right\} \tag{3.47}$$

$$\left.\begin{aligned} \Upsilon_{1n} = -\omega\left(H_{1n}^2 + 1\right)/\gamma_n, \qquad \Upsilon_{2n} = -\omega\left(H_{2n}^2 - H_{3n}^2 + 1\right)/\gamma_n, \\ \Upsilon_{3n} = -\omega(2H_{2n}H_{3n})/\gamma_n. \end{aligned}\right\} \tag{3.48}$$

(c) General solution

Adding the particular solution to the complementary solution gives us the general solution to (2.12)–(2.15). Let us truncate the series in these solutions to a finite number of terms. The axial velocity is

$$\begin{aligned} u(y,z) &= u_p + u_c \\ &= -\left(\frac{\kappa^4\zeta_1}{\kappa^4+\omega^2}\right)\frac{\cosh(\kappa z)}{\cosh(\kappa)} + \sum_{n=1}^{M} U_n \frac{\cosh(\beta_n y)}{\cosh(\beta_n b)}\cos(\alpha_n z) \\ &\quad + \sum_{n=1}^{M} U_{1n}(y)\cos(\alpha_n z) + \sum_{n=1}^{N} U_{2n}(z)\cos(\gamma_n y), \end{aligned} \tag{3.49}$$

where U_n, U_{1n} and U_{2n} are given in (3.5), (3.28) and (3.42), respectively. The transverse velocity is

$$\begin{aligned} v(y,z) &= v_p + v_c \\ &= -\left(\frac{\omega\kappa^2\zeta_1}{\kappa^4+\omega^2}\right)\frac{\cosh(\kappa z)}{\cosh(\kappa)} + \sum_{n=1}^{M} V_n \frac{\cosh(\beta_n y)}{\cosh(\beta_n b)}\cos(\alpha_n z) \\ &\quad + \sum_{n=1}^{M} V_{1n}(y)\cos(\alpha_n z) + \sum_{n=1}^{N} V_{2n}(z)\cos(\gamma_n y), \end{aligned} \tag{3.50}$$

where V_n, V_{1n} and V_{2n} are given in (3.6), (3.29) and (3.43), respectively. The vertical velocity is

$$\begin{aligned} w(y,z) &= w_p + w_c \\ &= \sum_{n=1}^{M} W_n \frac{\sinh(\beta_n y)}{\cosh(\beta_n b)}\sin(\alpha_n z) \\ &\quad + \sum_{n=1}^{M} W_{1n}(y)\sin(\alpha_n z) + \sum_{n=1}^{N} W_{2n}(z)\sin(\gamma_n y), \end{aligned} \tag{3.51}$$

where W_n, W_{1n} and W_{2n} are given in (3.7), (3.30) and (3.44), respectively. The pressure is

$$\begin{aligned} p(y,z) &= p_p + p_c \\ &= \sum_{n=1}^{M} P_n \frac{\sinh(\beta_n y)}{\cosh(\beta_n b)}\cos(\alpha_n z) \\ &\quad + \sum_{n=1}^{M} P_{1n}(y)\cos(\alpha_n z) + \sum_{n=1}^{N} P_{2n}(z)\sin(\gamma_n y), \end{aligned} \tag{3.52}$$

where P_n, P_{1n} and P_{2n} are given in (3.8), (3.31) and (3.45), respectively. We shall take $N \approx \mathrm{Int}(bM)$ so that the number of eigen-components in one direction is scaled by the length of the domain in that direction.

While the net flux is zero in the transverse and vertical directions, the axial volume flow rate through the channel is given by

$$\begin{aligned} Q &= 4\int_0^1\int_0^b u(y,z)\mathrm{d}y\mathrm{d}z \\ &= -\frac{4b\kappa^3\zeta_1\tanh(\kappa)}{\kappa^4+\omega^2} + 4\sum_{n=1}^{M}\left[U_n\frac{\tanh(\beta_n b)}{\beta_n} + C_{1n}\frac{\tanh(\lambda_{1n}b)}{\lambda_{1n}}\right. \\ &\quad + C_{2n}\frac{\sigma_{1n}\tanh(\sigma_{1n}b)\cos(\xi_{1n}b)+\xi_{1n}\sin(\xi_{1n}b)}{\sigma_{1n}^2+\xi_{1n}^2} \\ &\quad \left. + C_{3n}\frac{\sigma_{1n}\coth(\sigma_{1n}b)\sin(\xi_{1n}b)-\xi_{1n}\cos(\xi_{1n}b)}{\sigma_{1n}^2+\xi_{1n}^2}\right]\frac{(-1)^{n+1}}{\alpha_n} \\ &\quad + 4\sum_{n=1}^{N}\left[C_{4n}\frac{\tanh(\lambda_{2n})}{\lambda_{2n}}\right. \\ &\quad + C_{5n}\frac{\sigma_{2n}\tanh(\sigma_{2n})\cos(\xi_{2n})+\xi_{2n}\sin(\xi_{2n})}{\sigma_{2n}^2+\xi_{2n}^2} \\ &\quad \left. + C_{6n}\frac{\sigma_{2n}\coth(\sigma_{2n})\sin(\xi_{2n})-\xi_{2n}\cos(\xi_{2n})}{\sigma_{2n}^2+\xi_{2n}^2}\right]\frac{(-1)^{n+1}}{\gamma_n}. \end{aligned} \tag{3.53}$$

(d) Determining the coefficients

The remaining task is to determine the $3(M+N)$ coefficients $C_{1n},\cdots,C_{6n}$. This is accomplished by imposing the six no-slip boundary conditions: $u(b,z)=0$, $v(b,z)=0$, $w(b,z)=0$, $u(y,1)=0$, $v(y,1)=0$, and $w(y,1)=0$. Equations for the coefficients are developed as below, where we apply the orthogonality of the eigenfunctions to each of these boundary conditions.

For $m=1,\cdots,M$, on multiplying $u(b,z)=0$ and $v(b,z)=0$ by $\cos(\alpha_m z)$, which are then integrated with respect to z from 0 to 1, we get

$$C_{1m}+\cos(\xi_{1m}b)C_{2m}+\sin(\xi_{1m}b)C_{3m} = (-1)^{m+1}\left(\frac{2\kappa^4\zeta_1}{\kappa^4+\omega^2}\right)\left(\frac{\alpha_m}{\beta_m^2}\right) - U_m, \tag{3.54}$$

$$\begin{aligned} &F_{1m}C_{1m} + \left[F_{2m}\cos(\xi_{1m}b) + F_{3m}\tanh(\sigma_{1m}b)\sin(\xi_{1m}b)\right]C_{2m} \\ &\quad + \left[F_{2m}\sin(\xi_{1m}b) - F_{3m}\coth(\sigma_{1m}b)\cos(\xi_{1m}b)\right]C_{3m} \\ &\quad = (-1)^{m+1}\left(\frac{2\omega\kappa^2\zeta_1}{\kappa^4+\omega^2}\right)\left(\frac{\alpha_m}{\beta_m^2}\right) - V_m, \end{aligned} \tag{3.55}$$

where F_{1m}, F_{2m}, F_{3m} are given in (3.32).

For $m=1,\cdots,M$, on multiplying $w(b,z)=0$ by $\sin(\alpha_m z)$, which is then integrated with respect to z from 0 to 1, we get

$$\begin{aligned} &G_{1m}\tanh(\lambda_{1m}b)C_{1m} + \left[G_{2m}\tanh(\sigma_{1m}b)\cos(\xi_{1m}b) + G_{3m}\sin(\xi_{1m}b)\right]C_{2m} \\ &\quad + \left[G_{2m}\coth(\sigma_{1m}b)\sin(\xi_{1m}b) - G_{3m}\cos(\xi_{1m}b)\right]C_{3m} \\ &\quad + \sum_{n=1}^{N}\left[J_{1mn}C_{4n} + J_{2mn}C_{5n} + J_{3mn}C_{6n}\right] = -W_m\tanh(\beta_m b), \end{aligned} \tag{3.56}$$

where G_{1m}, G_{2m}, G_{3m} are given in (3.33),

$$J_{1mn} = (-1)^{m+n}I_{1n}\left(\frac{2\lambda_{2n}}{\alpha_m^2+\lambda_{2n}^2}\right), \tag{3.57}$$

$$
\begin{aligned}
J_{2mn} \;=\; & (-1)^{n+1}\left\{ I_{2n}\frac{\sigma_{2n}\sin(\alpha_m-\xi_{2n})-(\alpha_m-\xi_{2n})\tanh(\sigma_{2n})\cos(\alpha_m-\xi_{2n})}{(\alpha_m-\xi_{2n})^2+\sigma_{2n}^2}\right.\\
& + I_{2n}\frac{\sigma_{2n}\sin(\alpha_m+\xi_{2n})-(\alpha_m+\xi_{2n})\tanh(\sigma_{2n})\cos(\alpha_m+\xi_{2n})}{(\alpha_m+\xi_{2n})^2+\sigma_{2n}^2}\\
& + I_{3n}\frac{(\alpha_m-\xi_{2n})\sin(\alpha_m-\xi_{2n})+\sigma_{2n}\tanh(\sigma_{2n})\cos(\alpha_m-\xi_{2n})}{(\alpha_m-\xi_{2n})^2+\sigma_{2n}^2}\\
& \left. - I_{3n}\frac{(\alpha_m+\xi_{2n})\sin(\alpha_m+\xi_{2n})+\sigma_{2n}\tanh(\sigma_{2n})\cos(\alpha_m+\xi_{2n})}{(\alpha_m+\xi_{2n})^2+\sigma_{2n}^2}\right\}, \qquad (3.58)
\end{aligned}
$$

and

$$
\begin{aligned}
J_{3mn} \;=\; & (-1)^{n+1}\left\{ I_{2n}\frac{\sigma_{2n}\cos(\alpha_m-\xi_{2n})+(\alpha_m-\xi_{2n})\coth(\sigma_{2n})\sin(\alpha_m-\xi_{2n})}{(\alpha_m-\xi_{2n})^2+\sigma_{2n}^2}\right.\\
& - I_{2n}\frac{\sigma_{2n}\cos(\alpha_m+\xi_{2n})+(\alpha_m+\xi_{2n})\coth(\sigma_{2n})\sin(\alpha_m+\xi_{2n})}{(\alpha_m+\xi_{2n})^2+\sigma_{2n}^2}\\
& + I_{3n}\frac{(\alpha_m-\xi_{2n})\cos(\alpha_m-\xi_{2n})-\sigma_{2n}\coth(\sigma_{2n})\sin(\alpha_m-\xi_{2n})}{(\alpha_m-\xi_{2n})^2+\sigma_{2n}^2}\\
& \left. + I_{3n}\frac{(\alpha_m+\xi_{2n})\cos(\alpha_m+\xi_{2n})-\sigma_{2n}\coth(\sigma_{2n})\sin(\alpha_m+\xi_{2n})}{(\alpha_m+\xi_{2n})^2+\sigma_{2n}^2}\right\}. \qquad (3.59)
\end{aligned}
$$

For $m=1,\cdots,N$, on multiplying $u(y,1)=0$ and $v(y,1)=0$ by $\cos(\gamma_m y)$, which are then integrated with respect to y from 0 to b, we get

$$
C_{4m}+\cos(\xi_{2m})C_{5m}+\sin(\xi_{2m})C_{6m}=(-1)^{m+1}\left[\frac{2\kappa^4\zeta_1}{(\kappa^4+\omega^2)\,\gamma_m b}\right], \qquad (3.60)
$$

$$
\begin{aligned}
& H_{1m}C_{4m}+\left[H_{2m}\cos(\xi_{2m})+H_{3m}\tanh(\sigma_{2m})\sin(\xi_{2m})\right]C_{5m}\\
& \quad +\left[H_{2m}\sin(\xi_{2m})-H_{3m}\coth(\sigma_{2m})\cos(\xi_{2m})\right]C_{6m}=(-1)^{m+1}\left[\frac{2\omega\kappa^2\zeta_1}{(\kappa^4+\omega^2)\,\gamma_m b}\right], \qquad (3.61)
\end{aligned}
$$

where H_{1m}, H_{2m}, H_{3m} are given in (3.46).

For $m=1,\cdots,N$, on multiplying $w(y,1)=0$ by $\sin(\gamma_m y)$, which is then integrated with respect to y from 0 to b, we get

$$
\begin{aligned}
& \sum_{n=1}^{M}\left[K_{1mn}C_{1n}+K_{2mn}C_{2n}+K_{3mn}C_{3n}\right]\\
& \quad + I_{1m}\tanh(\lambda_{2m})C_{4m}+\left[I_{2m}\tanh(\sigma_{2m})\cos(\xi_{2m})+I_{3m}\sin(\xi_{2m})\right]C_{5m}\\
& \quad +\left[I_{2m}\coth(\sigma_{2m})\sin(\xi_{2m})-I_{3m}\cos(\xi_{2m})\right]C_{6m}=\sum_{n=1}^{M}(-1)^{m+n+1}\frac{2\beta_n W_n}{\left(\gamma_m^2+\beta_n^2\right)b}, \qquad (3.62)
\end{aligned}
$$

where I_{1m}, I_{2m}, I_{3m} are given in (3.47),

$$
K_{1mn}=(-1)^{m+n}G_{1n}\left[\frac{2\lambda_{1n}}{\left(\gamma_m^2+\lambda_{1n}^2\right)b}\right], \qquad (3.63)
$$

$$K_{2mn} = \frac{(-1)^{n+1}}{b} \times \left\{ G_{2n} \frac{\sigma_{1n} \sin[(\gamma_m - \xi_{1n})b] - (\gamma_m - \xi_{1n}) \tanh(\sigma_{1n} b) \cos[(\gamma_m - \xi_{1n})b]}{(\gamma_m - \xi_{1n})^2 + \sigma_{1n}^2} + G_{2n} \frac{\sigma_{1n} \sin[(\gamma_m + \xi_{1n})b] - (\gamma_m + \xi_{1n}) \tanh(\sigma_{1n} b) \cos[(\gamma_m + \xi_{1n})b]}{(\gamma_m + \xi_{1n})^2 + \sigma_{1n}^2} + G_{3n} \frac{(\gamma_m - \xi_{1n}) \sin[(\gamma_m - \xi_{1n})b] + \sigma_{1n} \tanh(\sigma_{1n} b) \cos[(\gamma_m - \xi_{1n})b]}{(\gamma_m - \xi_{1n})^2 + \sigma_{1n}^2} - G_{3n} \frac{(\gamma_m + \xi_{1n}) \sin[(\gamma_m + \xi_{1n})b] + \sigma_{1n} \tanh(\sigma_{1n} b) \cos[(\gamma_m + \xi_{1n})b]}{(\gamma_m + \xi_{1n})^2 + \sigma_{1n}^2} \right\}, \tag{3.64}$$

and

$$K_{3mn} = \frac{(-1)^{n+1}}{b} \times \left\{ G_{2n} \frac{\sigma_{1n} \cos[(\gamma_m - \xi_{1n})b] + (\gamma_m - \xi_{1n}) \coth(\sigma_{1n} b) \sin[(\gamma_m - \xi_{1n})b]}{(\gamma_m - \xi_{1n})^2 + \sigma_{1n}^2} - G_{2n} \frac{\sigma_{1n} \cos[(\gamma_m + \xi_{1n})b] + (\gamma_m + \xi_{1n}) \coth(\sigma_{1n} b) \sin[(\gamma_m + \xi_{1n})b]}{(\gamma_m + \xi_{1n})^2 + \sigma_{1n}^2} + G_{3n} \frac{(\gamma_m - \xi_{1n}) \cos[(\gamma_m - \xi_{1n})b] - \sigma_{1n} \coth(\sigma_{1n} b) \sin[(\gamma_m - \xi_{1n})b]}{(\gamma_m - \xi_{1n})^2 + \sigma_{1n}^2} + G_{3n} \frac{(\gamma_m + \xi_{1n}) \cos[(\gamma_m + \xi_{1n})b] - \sigma_{1n} \coth(\sigma_{1n} b) \sin[(\gamma_m + \xi_{1n})b]}{(\gamma_m + \xi_{1n})^2 + \sigma_{1n}^2} \right\}. \tag{3.65}$$

Equations (3.54)–(3.56) and (3.60)–(3.62) constitute $3(M+N)$ equations for the same number of unknowns: C_{1m}, C_{2m}, C_{3m}, where $m = 1, \cdots, M$, and C_{4m}, C_{5m}, C_{6m}, where $m = 1, \cdots, N$. We may first solve (3.54) and (3.55) for C_{2m} and C_{3m} such that they are expressed in terms of C_{1m}. Similarly, we may solve (3.60) and (3.61) for C_{5m} and C_{6m} such that they are expressed in terms of C_{4m}. We then substitute these expressions into (3.56) and (3.62) to form a reduced system of $M+N$ equations involving C_{1m} and C_{4m} as the unknowns only. This system of equations can be solved by using a standard linear algebraic equation solver.

4. Limiting cases

(a) Non-rotating channel

When the channel is not rotating or $\omega = 0$, the secondary flow is identically zero $(v, w) \equiv 0$. The axial velocity is readily found to be

$$u(y,z) = \zeta_1 - \psi(y,z) + 2(\zeta_1 - \zeta_2) \sum_{n=1}^{\infty} \frac{(-1)^n}{\alpha_n} \frac{\cosh(\alpha_n y)}{\cosh(\alpha_n b)} \cos(\alpha_n z) \qquad \text{for } \omega = 0, \tag{4.1}$$

where $\psi(y,z)$ is given in (2.17). The axial flow rate in this case is

$$Q_{\rm nr} = 4b\zeta_1 \left(1 - \frac{\tanh(\kappa)}{\kappa}\right) - 8 \sum_{n=1}^{\infty} \left(\zeta_2 - \frac{\alpha_n^2}{\beta_n^2} \zeta_1\right) \frac{\tanh(\beta_n b)}{\alpha_n^2 \beta_n} - 8(\zeta_1 - \zeta_2) \sum_{n=1}^{\infty} \frac{\tanh(\alpha_n b)}{\alpha_n^3}. \tag{4.2}$$

(b) Very wide channel

Consider the limiting case of a very wide channel ($b \gg 1$), for which the dependence of the problem on y can be ignored as long as it is not too close to the side walls. Therefore, $u = u(z)$, $v = v(z)$ and $w \equiv 0$. The problem then simplifies to

$$-\omega v = \frac{\mathrm{d}^2 u}{\mathrm{d}z^2} + \kappa^2 \psi, \tag{4.3}$$

$$\omega u = -\frac{\mathrm{d}p}{\mathrm{d}y} + \frac{\mathrm{d}^2 v}{\mathrm{d}z^2}, \tag{4.4}$$

where $\psi(z) = \cosh(\kappa z)/\cosh(\kappa)$ on taking $\zeta_1 = 1$. The pressure p, as dictated by the z-momentum, is independent of z, and can only vary linearly with y such that its gradient in this direction, $K_y \equiv -\mathrm{d}p/\mathrm{d}y$, is a constant. Note that this limiting case corresponds to rotating EOF between two parallel plates with lateral confinement. Despite a long width, the net flux in the transverse direction is always zero, which is the condition by which K_y is to be determined. In this regard, the problem here is different from that studied by Chang & Wang [2], who looked into rotating EOF between two infinite parallel plates without lateral confinement. In their problem, K_y is zero, allowing net flow to happen in both axial and transverse directions.

The general solution to (4.3) and (4.4) is

$$u(z) = \frac{K_y}{\omega} - A\frac{\cosh(\kappa z)}{\cosh(\kappa)} + c_1 \cosh(\eta z)\cos(\eta z) + c_2 \sinh(\eta z)\sin(\eta z), \tag{4.5}$$

$$v(z) = -B\frac{\cosh(\kappa z)}{\cosh(\kappa)} + c_1 \sinh(\eta z)\sin(\eta z) - c_2 \cosh(\eta z)\cos(\eta z), \tag{4.6}$$

where $\eta = (\omega/2)^{1/2}$, and

$$A = \frac{\kappa^4}{\kappa^4 + \omega^2}, \qquad B = \frac{\omega\kappa^2}{\kappa^4 + \omega^2}. \tag{4.7}$$

Using the no-slip and zero flux conditions: $u(1) = v(1) = \int_0^1 v\mathrm{d}z = 0$, we may determine that

$$c_1 = \frac{(-K_y/\omega + A)\cosh(\eta)\cos(\eta) + B\sinh(\eta)\sin(\eta)}{\cosh^2(\eta)\cos^2(\eta) + \sinh^2(\eta)\sin^2(\eta)}, \tag{4.8}$$

$$c_2 = \frac{(-K_y/\omega + A)\sinh(\eta)\sin(\eta) - B\cosh(\eta)\cos(\eta)}{\cosh^2(\eta)\cos^2(\eta) + \sinh^2(\eta)\sin^2(\eta)}, \tag{4.9}$$

$$\begin{aligned} \frac{K_y}{\omega} &= A + B\frac{\sinh(\eta)\cosh(\eta) + \sin(\eta)\cos(\eta)}{\sin(\eta)\cos(\eta) - \sinh(\eta)\cosh(\eta)} \\ &\quad - C\frac{\cosh^2(\eta)\cos^2(\eta) + \sinh^2(\eta)\sin^2(\eta)}{\sin(\eta)\cos(\eta) - \sinh(\eta)\cosh(\eta)}, \end{aligned} \tag{4.10}$$

where

$$C = \frac{\omega\sqrt{2\omega}\kappa\tanh(\kappa)}{\kappa^4 + \omega^2}. \tag{4.11}$$

The axial flow rate per unit width is then given by

$$\begin{aligned} q &= 2\int_0^1 u\mathrm{d}z \\ &= 2\left[\frac{K_y}{\omega} - A\frac{\tanh(\kappa)}{\kappa}\right] + \frac{c_1}{\eta}\left[\cosh(\eta)\sin(\eta) + \sinh(\eta)\cos(\eta)\right] \\ &\quad + \frac{c_2}{\eta}\left[\cosh(\eta)\sin(\eta) - \sinh(\eta)\cos(\eta)\right]. \end{aligned} \tag{4.12}$$

We show in figure 2 some velocity profiles $u(z)$, $v(z)$ for rotating EOF in a very wide channel. In view of symmetry about $z = 0$, only the profiles in the upper half of the channel ($0 \le z \le 1$) are shown. When $\omega = 0$, the axial flow is the pure EOF: a plug-like flow profile in the core region,

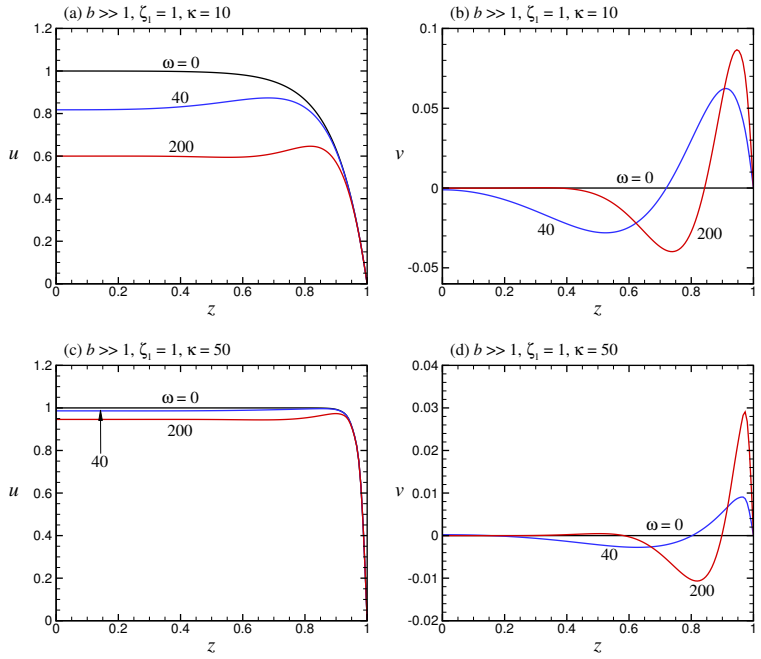

Figure 2. Axial and transverse velocity profiles $u(z)$, $v(z)$ in a very wide channel $b \gg 1$, where (*a*) $u(z)$ for $\kappa = 10$, (*b*) $v(z)$ for $\kappa = 10$, (*c*) $u(z)$ for $\kappa = 50$, (*d*) $v(z)$ for $\kappa = 50$.

where the velocity is the Helmholtz–Smoluchowski velocity. For $\omega \neq 0$, the following points are noteworthy. First, as ω increases (i.e. faster rotation), the axial velocity decreases, while keeping a uniform profile, in the core region of the channel. The axial velocity will as a result attain a maximum value somewhere between the near-wall sheared region and the interior uniform region. The rotation-induced velocity profile seen here (i.e. an overshoot followed by a uniform flow in the interior) is similar to that found in pressure-driven rotating channel flow (e.g. Hart [17]; Speziale [18]; Kheshgi & Scriven [19]; Nandakumar *et al.* [20]). Second, for higher κ (i.e. a thinner EDL), the axial flow has a larger plug flow region, where the flow is less susceptible to the decreasing effect of ω. This means that the Coriolis force will have less effect on an EOF with a larger Debye parameter. Third, the transverse velocity turns from positive near the wall to negative before diminishing to zero toward the center. Unless ω and κ are sufficiently large, v is not as uniformly distributed as u in the interior region. Of course, owing to confinement of the channel in the transverse direction, v is in general much smaller in magnitude than u. As κ increases, v drops off more quickly to zero in the interior, amounting to a diminished Coriolis force for the axial flow; see (4.3). This also explains why rotation will have a weaker effect on EOF with a thinner EDL.

To further illustrate our points mentioned above, we show in figure 3 the flow rate per unit width, q, as a function of ω and κ. As ω increases, q decreases for any κ. This conforms to the classical understanding that rotation will increase the resistance to flow [21]. This decreasing effect due to rotation on the flow rate is, however, weaker for larger κ; see the explanations given above. For the cases shown in this figure, the reduction in q at $\omega = 200$ is 71.5%, 35.6%, 4.9% for $\kappa = 1$, 10, 50, respectively.

(c) Ekman–EDL layer

The flow profiles shown in figure 2 reveal that a boundary layer structure will be exhibited when ω is sufficiently large. Let us examine this in greater detail. In addition to the condition of a very

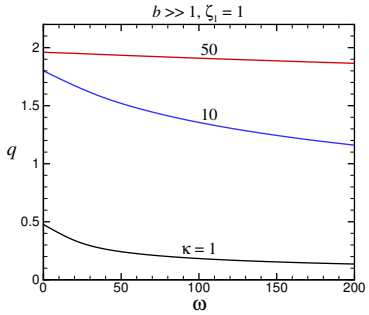

Figure 3. Flow rate per unit width q in a very wide channel $b \gg 1$ as a function of the rotation parameter ω.

wide channel ($b \gg 1$), we now further assume that the rotation is so fast and the EDL is so thin that $\omega^{1/2} \gg 1$ and $\kappa \gg 1$. As a consequence, the balance between the viscous force, electric body force, pressure gradient and Coriolis force will be confined to a thin layer near each of the two horizontal walls. This is essentially Coriolis force in an Ekman layer interacting with electrokinetics in an EDL, and therefore we shall call such a layer an Ekman–EDL layer. Outside this layer, where the viscous force and the electric body force vanish, the flow is geostrophic (i.e. a mere balance between pressure gradient and Coriolis force).

As is well known, an Ekman layer is scaled by the square root of the Ekman number, while an EDL is scaled by the inverse Debye parameter. In terms of the present notation, these scales are $\omega^{-1/2}$ and κ^{-1}, respectively. Our discussion here is based on the condition that these two scales are small parameters of the same order of magnitude.

To fix ideas let us examine in particular the Ekman–EDL layer that develops on the upper wall. Recalling from (2.19) that $\eta \equiv (\omega/2)^{1/2} = h/\delta_E$, we first define a stretched local coordinate

$$z^* = \eta(1 - z), \tag{4.13}$$

which is the distance from the upper wall into the fluid. We also introduce a modified non-dimensional Debye parameter, which is the Debye parameter normalized by the Ekman layer thickness instead of the channel height,

$$\kappa^* = \kappa/\eta. \tag{4.14}$$

For $\kappa \gg 1$, the electric potential near the upper wall reduces to $\psi = \exp(-\kappa^* z^*)$. Together with $\eta \gg 1$, we may readily obtain from (4.5) and (4.6) the following asymptotic limits applicable to flow in an Ekman–EDL layer:

$$u(z^*) = \frac{K_y}{\omega} - A^* \mathrm{e}^{-\kappa^* z^*} + \mathrm{e}^{-z^*} \left[B^* \sin(z^*) + C^* \cos(z^*) \right], \tag{4.15}$$

$$v(z^*) = -B^* \mathrm{e}^{-\kappa^* z^*} + \mathrm{e}^{-z^*} \left[B^* \cos(z^*) - C^* \sin(z^*) \right], \tag{4.16}$$

where $K_y = -\mathrm{d}p/\mathrm{d}y$,

$$A^* = \frac{\kappa^{*4}}{\kappa^{*4} + 4}, \qquad B^* = \frac{2\kappa^{*2}}{\kappa^{*4} + 4}, \qquad C^* = \frac{2\kappa^{*2} - 4\kappa^*}{\kappa^{*4} + 4}, \tag{4.17}$$

and

$$\frac{K_y}{\omega} = A^* - C^* = \frac{\kappa^{*4} - 2\kappa^{*2} + 4\kappa^*}{\kappa^{*4} + 4}. \tag{4.18}$$

It is remarkable that the flow structure in an Ekman–EDL layer is characterised by, in addition to the Ekman number, the parameter κ^*, which is the Debye parameter normalized by the Ekman layer thickness. This parameter distinguishes an Ekman–EDL layer from an Ekman layer, which is characterised by the Ekman number alone.

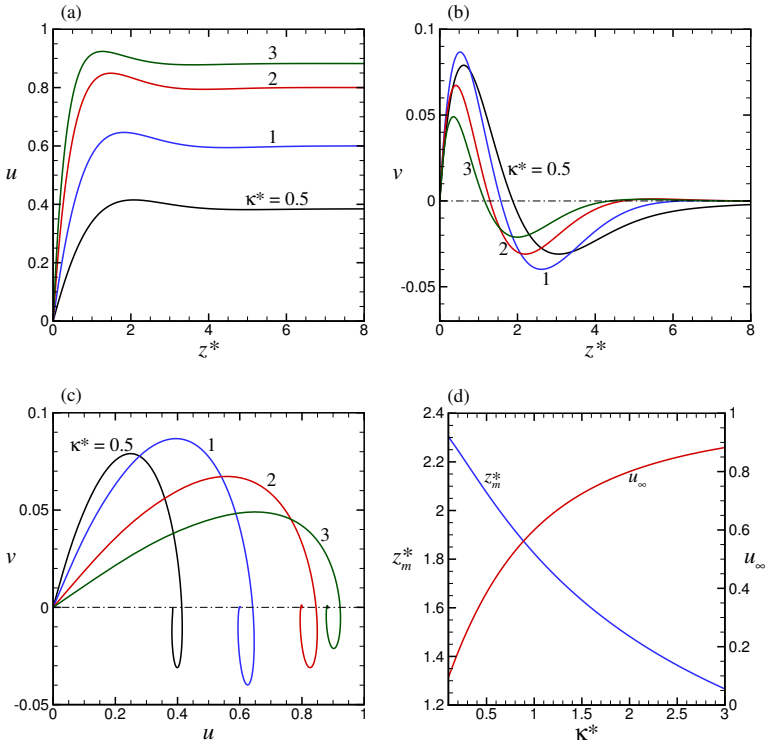

Figure 4. For flow in an Ekman–EDL layer: (*a*) axial velocity profiles $u(z^*)$, (*b*) transverse velocity profiles $v(z^*)$, (*c*) Ekman spirals, (*d*) z^*_m and u_∞ as functions of κ^*, where z^*_m is the height at which u is the maximum, and u_∞ is the limit of u as $z^* \to \infty$.

We show in figure 4(*a*, *b*), for some values of κ^*, the axial and transverse velocity profiles in an Ekman–EDL layer. The corresponding Ekman spirals are shown in figure 4(*c*). The axial velocity profiles exhibit an overshoot, which is often found in an Ekman layer, as has been remarked above. The axial velocity reaches the maximum at $z^* = z^*_m$, i.e. $u(z^*_m) = u_{\max}$, where z^*_m is given by the smallest positive root of the following equation:

$$\kappa^{*4} \mathrm{e}^{-(\kappa^*-1)z^*_m} + 4\left[\cos(z^*_m) - (\kappa^* - 1)\sin(z^*_m)\right] = 0. \tag{4.19}$$

As shown in figure 4(*d*), z^*_m decreases monotonically as κ^* increases. In other words, the peak axial velocity will be closer to the wall as the EDL becomes thinner or the Ekman layer becomes thicker.

At a large distance from the wall, the velocity components tend to the following limits:

$$\lim_{z^* \to \infty} (u,\, v) = (K_y/\omega,\, 0), \tag{4.20}$$

which is the geostrophic velocity for the region outside the Ekman–EDL layer. A formal proof [16] shows that, for a rotation $\vec{\Omega} = \Omega\vec{k}$, the geostrophic approximation to the full momentum equation leads to the following result (in terms of dimensional quantities):

$$\vec{u}_\perp = \frac{\vec{k} \times \nabla p}{2\rho\Omega}, \tag{4.21}$$

where $\vec{k}$ is the unit vector along $\vec{\Omega}$, and $\vec{u}_\perp$ is the velocity perpendicular to $\vec{\Omega}$. The geostrophic velocity, as given above, is perpendicular to the pressure gradient. In other words, the geostrophic flow is along, but not across, lines of constant pressure. In the present problem, the axial

geostrophic flow is driven by the transverse pressure gradient, which is induced in order to balance the mass flux in the transverse direction. On the other hand, the transverse geostrophic flow is zero simply because of the absence of a pressure gradient along the axial direction. One should note that although the flow in an Ekman layer is generated under the effect of viscosity, the velocity at the outer edge of the Ekman layer is independent of viscosity.

Denoting K_y/ω by u_∞, the geostrophic limit of the axial velocity as a function of κ^*, as given in (4.18), is shown also in figure 4(*d*). Note that u_∞ is always positive, increasing monotonically with κ^*, and approaching the upper limit of unity as $\kappa^* \to \infty$. This again corresponds to the fact that when the EDL becomes much thinner than the Ekman layer, the velocity of the inviscid core flow is essentially the Helmholtz–Smoluchowski velocity. The Coriolis force will lose its influence then, as has been remarked above. Conversely, when the EDL is thicker than the Ekman layer, the geostrophic velocity can dwindle appreciably, becoming a small fraction of the Helmholtz–Smoluchowski velocity only. For a moderate value of κ, u_∞ may be sensitively decreased by increasing ω.

The lateral confinement is to induce a positive $K_y \equiv -\mathrm{d}p/\mathrm{d}y$, or a favourable transverse pressure gradient. This accords with the fact that, without the lateral confinement, the transverse flow is always negative, as has been found by Chang & Wang [2]. A favourable pressure gradient is needed in order to cause part of the flow to be positive, thereby counterbalancing the remaining negative part of the flow. As can be seen from figure 4(*b*), the transverse flow is always positive near the wall. From the Ekman spirals shown in figure 4(*c*), it is also seen that the transverse velocity turns from positive to negative at a point very close to where the axial velocity is the maximum.

The geostrophic approximation also implies the Taylor–Proudman theorem, which states that $(2\vec{\Omega}\cdot\nabla)\vec{u} = 0$ when the Rossby number, viscous effect and baroclinicity are all very small [16]. When this theorem is satisfied, all the velocity components will be independent of the direction parallel to the rotation axis. In the present problem, the Taylor–Proudman theorem is obviously applicable in the region outside an Ekman–EDL layer, where the axial velocity is uniform, thereby independent of z, and the transverse velocity is zero; see (4.20). Even for those velocity profiles of $\omega > 0$ shown in figure 2, the Taylor–Proudman theorem is satisfied to the leading order by the interior flow, where the axial velocity is essentially independent of z, while the transverse velocity, although not independent of z, is small by an order of magnitude.

5. Finite aspect ratio

We now consider rotating EOF in a channel of a finite aspect ratio $b = O(1)$, allowing us to look into the effects due to confinement by the side walls. Three cases of wall potential distributions are considered: (i) all walls are charged (AWC): $\zeta_1 = \zeta_2 = 1$; (ii) only the horizontal (i.e. top/bottom) walls are charged (HWC): $\zeta_1 = 1$, $\zeta_2 = 0$; (iii) only the vertical (i.e. side) walls are charged (VWC): $\zeta_1 = 0$, $\zeta_2 = 1$. By linearity, the flow under AWC is the sum of those under HWC and VWC. However, we will show that disparate dependence on the controlling parameters will be exhibited by EO flows under these three conditions.

It has long been known that rotation may decrease the rate of flow along a channel that rotates about an axis perpendicular to its own [21]. We have shown above that this statement applies to our problem for a very wide channel. In figure 5, we show how the flow rate Q may vary with the rotation parameter ω for different channel widths. For a relatively wide channel $b = 2$, Q decreases monotonically with ω under all conditions, which is consistent with our wide-channel-limit. For a unity aspect ratio $b = 1$, it is of interest to find that Q varies non-monotonically with ω when it is under HWC. The flow rate first increases with ω, attaining a maximum value at $\omega \approx 40$, and then decreases for higher values of ω. For a narrow channel ($b = 0.5$), the flow rate under HWC will increase monotonically with ω in the range shown in the figure. This opposite dependence on ω has made HWC stand in sharp contrast to the other two cases. For an even narrower channel ($b = 0.2$), the dependence of Q on ω continues to be increasing for HWC, while decreasing for AWC and VWC, but the change is so small that the effect of ω can be ignored for such a narrow

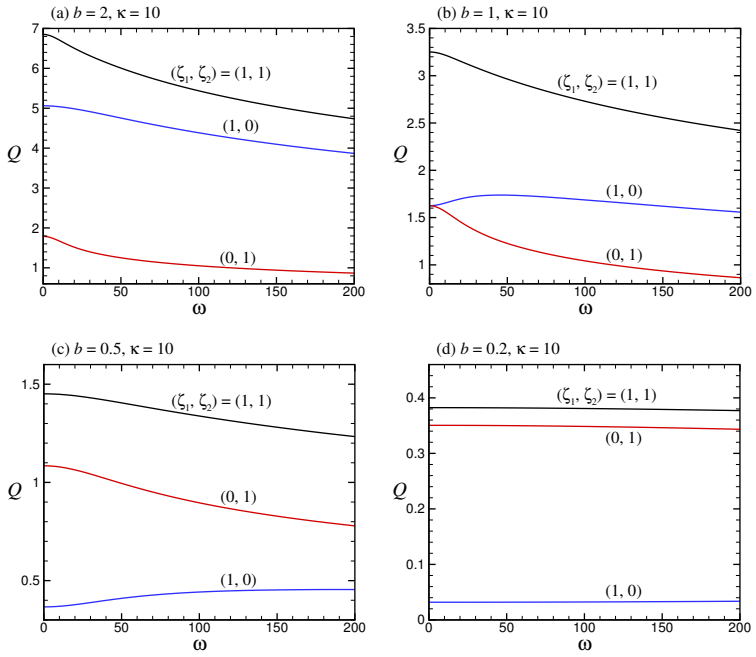

Figure 5. Flow rate Q in a channel of finite width as a function of the rotation parameter ω, where $\kappa = 10$, and (*a*) $b = 2$, (*b*) $b = 1$, (*c*) $b = 0.5$, (*d*) $b = 0.2$. Three cases are considered: all walls are charged (AWC) when $(\zeta_1, \zeta_2) = (1, 1)$, only vertical walls are charged (VWC) when $(\zeta_1, \zeta_2) = (0, 1)$, and only horizontal walls are charged (HWC) when $(\zeta_1, \zeta_2) = (1, 0)$.

channel. We shall provide physical explanations for these contrasting behaviours when we look into the axial and transverse flow fields in the following sections.

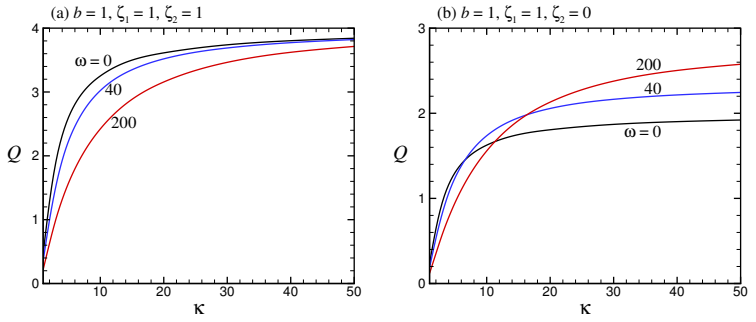

Figure 6. Flow rate Q in a square channel $b = 1$ as a function of the Debye parameter κ, for (*a*) AWC, (*b*) HWC.

We further show in figure 6 the effect of the Debye parameter κ on the flow rate Q in a channel of unity aspect ratio. When it is under AWC, Q decreases with increasing ω for any κ. The decreasing effect of ω on Q is most pronounced for $\kappa = O(10)$. For $\kappa \geq 30$ (i.e. a very thin EDL), Q will not be very sensitive to ω, which again is consistent with what we have found for a very wide channel. In sharp contrast, when it is under HWC, Q may change in different manners as a function of ω, depending on κ. For $\kappa = O(1)$, Q decreases with increasing ω. For $\kappa \sim 10$, Q changes non-monotonically with ω, as has already been seen in figure 5(*b*). For $\kappa \geq 20$,

the dependence is completely to the contrary: Q increases monotonically with ω, at least within the ranges of parameters shown in the figures. Also, unlike the case of AWC, Q may change more appreciably with ω for higher κ. Our results here reveal that when only the horizontal walls are charged and the EDL is sufficiently thin, rotation may enhance EOF in a channel of finite width. Such flow enhancement, or reduction of flow resistance, is opposite to what is commonly known about the effect of rotation on flow in a rotating duct.

(a) Axial flow

To have a better understanding about the effect of rotation, we show in figure 7 three-dimensional plots of the axial velocity distributions $u(y, z)$ for the cases AWC, VWC and HWC, where $\kappa = 10$, and $\omega = 0$, 40, 200. By symmetry, only one quarter of the channel cross-section is shown. In the case of AWC, shown in figure 7(*a–c*), an equal EO pumping from the EDLs on the four walls produces a plug flow in the core region. In the absence of background velocity shear there, the geostrophic condition is satisfied in the interior for any $\omega \neq 0$. Of course, a larger ω will lead to a lower geostrophic velocity. According to our results presented in §4(c), the velocity at the outer edge of an Ekman–EDL layer should decrease as $\kappa^* \equiv \kappa(2/\omega)^{1/2}$ decreases, as shown in figure 4(*d*). Hence, in this case, the rotation is to merely lower the geostrophic velocity according to $\omega^{-1/2}$, where the interior flow remains virtually uniform whether ω is zero or not (the uniform velocity being the Helmholtz–Smoluchowski velocity when $\omega = 0$).

In the case of VWC, shown in figure 7(*d–f*), the upper wall at $z = 1$ is uncharged, and therefore has no EO pumping near this boundary. As a result of frictional retardation at this boundary, the velocity profile is not uniform along the vertical centerline ($y = 0$) when $\omega = 0$: u decreases markedly from the maximum at the centre toward 0 at $z = 1$ (i.e. $\partial u/\partial z < 0$). Owing to this background velocity shear, the geostrophic condition or the Taylor–Proudman theorem is not satisfied in the interior for small ω. With sufficiently large ω, the Coriolis acceleration will eventually be strong enough to force a geostrophic flow that is independent of z to be materialised in the interior region (see our proof below). As constrained by the no-slip condition at $z = 1$, the tendency to attain a uniform profile in the z-direction will result in a lower velocity in the core region of the flow. The overall effect is a diminished flow rate through the channel.

In the case of HWC, shown in figure 7(*g–i*), the upper wall at $z = 1$ is charged, and therefore an EDL is formed there. Frictional retardation due to the uncharged lateral wall at $y = 1$ causes the velocity at the centre to be lower than the velocity at the outer edge of the EDL. As a result, in the absence of rotation ($\omega = 0$), the velocity profile along the vertical centerline ($y = 0$) slopes upward ($\partial u/\partial z > 0$) in the interior. Again, the side wall friction renders the Taylor–Proudman theorem invalid at small ω. With sufficiently fast rotation, the Coriolis effect will be strong enough to bring forth a profile that is independent of z in the interior (see our proof below). As this geostrophic velocity is to match the velocity at the outer edge of the Ekman–EDL layer, a uniform profile in the z-direction can be achieved only through an increase of the velocity in the core region. This explains the increased flow rate at $\omega = 40$; compare the profiles shown in figure 7(*g*, *h*). Since the velocity at the outer edge of the Ekman–EDL layer will decrease with increasing ω (see our discussion above), a further increase of ω may, however, lower the entire profile (i.e. the Ekman–EDL layer and the geostrophic core). This explains the decreased flow rate at $\omega = 200$; compare the profiles shown in figure 7(*h*, *i*).

Let us now find out how a Taylor–Proudman profile where $\partial u/\partial z$ is zero may develop in the interior as ω becomes large. Recall the dimensional form of the governing equations:

$$-2\rho\Omega v = \mu\nabla^2 u, \tag{5.1}$$

$$2\rho\Omega u = -\frac{\partial p}{\partial y} + \mu\nabla^2 v, \tag{5.2}$$

$$0 = -\frac{\partial p}{\partial z} + \mu\nabla^2 w, \tag{5.3}$$

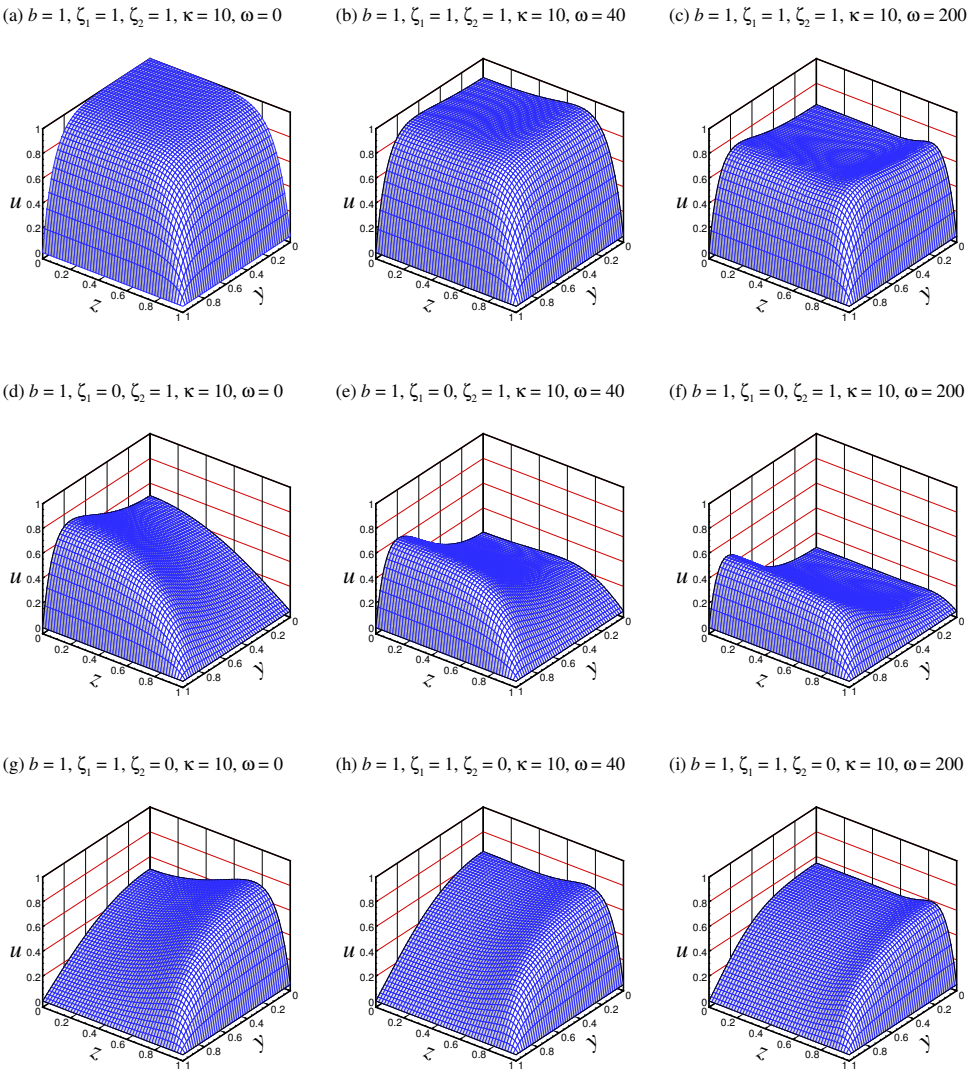

Figure 7. Axial velocity profiles $u(y, z)$ in a square channel $b = 1$, where $\kappa = 10$, and for AWC: (*a*) $\omega = 0$, (*b*) $\omega = 40$, (*c*) $\omega = 200$; for VWC: (*d*) $\omega = 0$, (*e*) $\omega = 40$, (*f*) $\omega = 200$; for HWC: (*g*) $\omega = 0$, (*h*) $\omega = 40$, (*i*) $\omega = 200$.

where the electric body force is omitted, and therefore these equations should apply in the region outside the EDL. Flow in the interior will be subject to shear when the walls are not all equally charged (e.g. HWC or VWC). The elimination of pressure from (5.2) and (5.3) gives the well-known equation

$$2\rho\Omega\frac{\partial u}{\partial z} = -\mu\nabla^2\chi \tag{5.4}$$

where $\chi = \partial w/\partial y - \partial v/\partial z$ is the axial component of the vorticity. The term on the left side is called by Hart [17] the vertical Coriolis torque, an x-vorticity source term responsible for the generation of secondary flow in a rotating channel. This term can also be interpreted, following Pedlosky [16], as the production of axial vorticity due to the tilting of the $\vec{\Omega}$ vorticity filament by the shear of the axial velocity. Hence, the equation above is to state that the viscous diffusion of χ is balanced by the tilting of the $\Omega\vec{k}$ vortex filament in the x-direction by $\partial u/\partial z$.

We use again half the channel height, h, as the characteristic length scale, and the Helmholtz–Smoluchowski velocity, U, given in (2.11) as the characteristic scale for the axial velocity u. It follows from (5.1) and the continuity equation that the characteristic scale for the secondary flow velocities $(v,\ w)$ is

$$V,\ W \sim \frac{\mu U}{2\rho\Omega h^2} = \frac{U}{\omega} \tag{5.5}$$

for $\omega \geq O(1)$. Then, from (5.4), we may estimate that

$$\frac{\partial u}{\partial z} \sim \left(\frac{\mu}{2\rho\Omega h^2}\right)^2 \frac{U}{h} = \frac{1}{\omega^2}\frac{U}{h}. \tag{5.6}$$

Therefore, when $\omega \gg 1$, the secondary flow velocity in the interior can only be an order $O(\omega^{-1})$ smaller than the axial velocity. More importantly, the velocity shear $\partial u/\partial z$ in the interior will diminish according to ω^{-2}. This provides us with a simple way to estimate to what extent a Taylor–Proudman interior flow will develop as a function of ω. Our profiles shown in figure 7 confirm that $\partial u/\partial z$ is practically zero in the interior when $\omega \geq O(10)$.

(b) Secondary flow

For the rotating cases shown in figure 7, their corresponding secondary flow fields are shown in figure 8. Solid and dashed lines are used to denote positive and negative values of the streamfunction $\varphi(y,z) = \int_0^z v\mathrm{d}z$. Also shown in the figure are the directions of flow looking upstream (i.e. the axial flow is out of the plane of the paper). Along a dashed streamline the circulation is clockwise, while along a solid streamline the circulation is counterclockwise. To get the flow pattern across the entire channel section, one should first form a mirror image of the streamlines about $y = 0$ (keeping the same sense of circulation in the image), and then form another image about $z = 0$.

Some salient points about the secondary flow fields are discussed as follows.

(i) AWC; figure 8(*a*, *b*)
For a moderate $\omega = 40$, the secondary flow as shown in figure 8(*a*) features a double-vortex configuration (one vortex located in the upper and lower half of the channel) that resembles what has long been known in the literature. This double-vortex, together with the sense of rotation, looks similar to those found experimentally or numerically by Hart [17], Speziale [18] and Kheshgi & Scriven [19], although the driving force and flow regimes studied by these authors are different from those of the present study. The Coriolis force is to throw the fast moving fluid in the channel core in the direction of the cross product of the mean flow velocity with the rotation vector $\vec{\Omega}$, i.e. toward the left wall when looking upstream [19]. For a higher $\omega = 200$, as shown in figure 8(*b*), a four-vortex configuration shows up. The vortex in one half of the channel divides itself into a dumb-bell-shaped pair of vortices, so that there is one vortex centre located in one quarter of the channel. The distribution of the vorticity is so much changed that the centre of the quadrant vortex is shifted toward the corner of the channel. This is a result of the following two effects. First, as ω increases, the transverse flow in the Ekman–EDL layer near $z = 1$ also increases (see figure 4), leading to a stronger Ekman pumping of secondary flow near the upper wall. Second, as ω increases, the Coriolis torque $\partial u/\partial z$ in the interior decreases, as has been discussed above. The diminishing of the vorticity source term leads to a virtually stagnant zone for the secondary flow in the interior.

(ii) VWC; figure 8(*c*, *d*)
While the flow patterns are largely the same as those for AWC, the secondary flow has a wider distribution and a stronger intensity in this case. Without EO pumping from the upper wall, the axial flow is subject to higher shear due to wall friction. As a result, stronger axial vorticity is generated from the upper wall, and diffuses more extensively

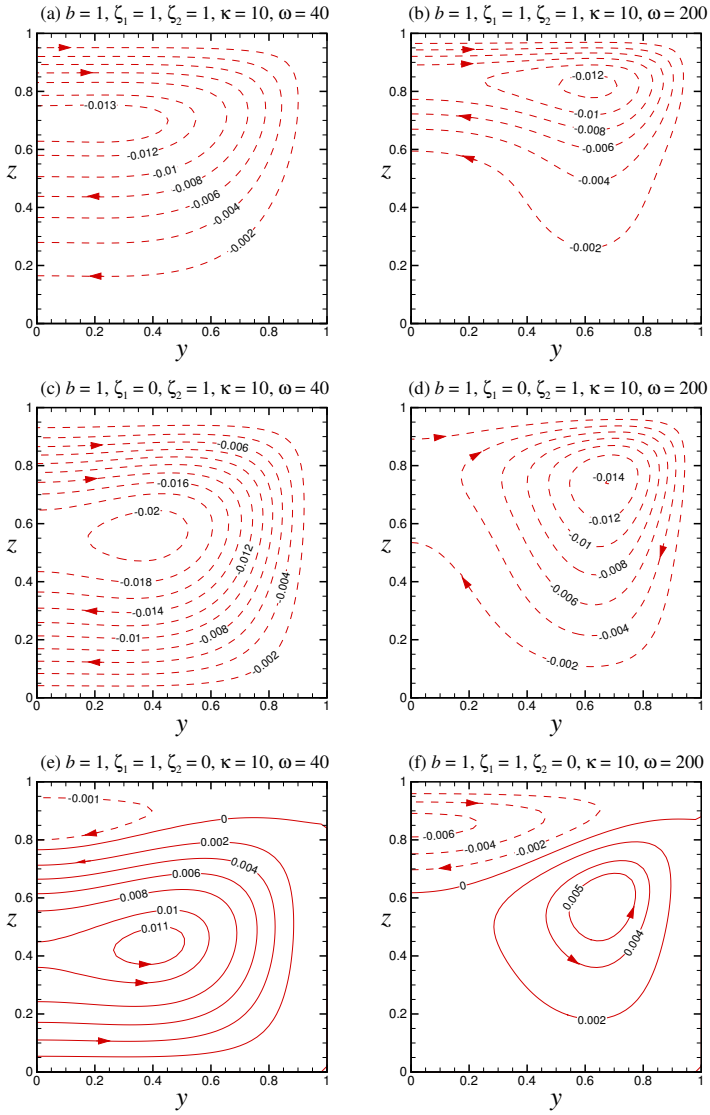

Figure 8. Streamlines showing the secondary flow fields in a square channel $b = 1$, where $\kappa = 10$, and for AWC: (*a*) $\omega = 40$, (*b*) $\omega = 200$; for VWC: (*c*) $\omega = 40$, (*d*) $\omega = 200$; for HWC: (*e*) $\omega = 40$, (*f*) $\omega = 200$.

into the inner part of the channel section. A well-formed quadrant vortex shows up in figure 8(*d*).

(iii) HWC; figure 8(*e*, *f*)

The flow patterns are dramatically different from those discussed above. While a clockwise vortex still persists near the Ekman–EDL layer at the upper wall, the secondary flow is now dominated by a counterclockwise vortex in the interior when $\omega = 40$. The reason for the generation of this vortex is as follows. Let us recall figure 5(*b*), from which it is seen that the flow rate increases as ω increases from 0 to 40. The increase in flow rate is essentially through an increase of the axial velocity in the interior, as has been shown in figure 7(*h*), in the course of approaching the Taylor–Proudman profile as ω increases. It follows from (5.2) that such an increase of the axial velocity can only be brought about by a higher favourable transverse gradient $-\partial p/\partial y$ in the interior. We have confirmed by checking our results that $-\partial p/\partial y$ at the centre $(0, 0)$, which is always positive, will

indeed increase in magnitude as ω increases from 0 to 40 in this case. As u decreases along the transverse direction, the Coriolis force slightly weakens away from the centre in this direction. The presence of a favourable pressure gradient in the y-direction will therefore produce a forward transverse flow near the center, thereby forming a counterclockwise vortex spanning across much of the channel section. For a higher $\omega = 200$, the upper clockwise vortex becomes more intensive and extensive, while the opposite is true for the lower counterclockwise vortex. Again, this is due to a stronger Ekman pumping near the upper wall, while a weaker source term in the interior, as ω gets larger.

Table 1. The ratios $Q/Q_{\rm nr}$, $|v|_{\max}/|u|_{\max}$, and $\bar{v}_{\rm sf}/\bar{u}$ for $\kappa = 10$. AWC = all walls are charged; VWC = only vertical walls are charged; HWC = only horizontal walls are charged.

			$Q/Q_{\rm nr}$		$\lvert v\rvert_{\max}/\lvert u\rvert_{\max}$ (%)		$\bar{v}_{\rm sf}/\bar{u}$ (%)	
b	Case	(ζ_1, ζ_2)	$\omega = 40$	$\omega = 200$	$\omega = 40$	$\omega = 200$	$\omega = 40$	$\omega = 200$
2	AWC	(1, 1)	0.898	0.691	7.75	15.51	2.88	3.27
	VWC	(0, 1)	0.736	0.485	11.87	20.00	13.10	11.09
	HWC	(1, 0)	0.955	0.764	6.79	13.31	3.26	3.37
1	AWC	(1, 1)	0.929	0.745	7.96	15.55	3.11	3.68
	VWC	(0, 1)	0.791	0.531	13.13	20.13	12.05	10.70
	HWC	(1, 0)	1.068	0.958	6.25	12.23	5.08	4.17
0.5	AWC	(1, 1)	0.977	0.850	7.49	16.79	3.16	4.49
	VWC	(0, 1)	0.939	0.718	15.64	25.50	10.51	10.47
	HWC	(1, 0)	1.090	1.240	13.96	13.61	16.50	8.15

Table 2. As Table 1, but for $\kappa = 50$.

			$Q/Q_{\rm nr}$		$\lvert v\rvert_{\max}/\lvert u\rvert_{\max}$ (%)		$\bar{v}_{\rm sf}/\bar{u}$ (%)	
b	Case	(ζ_1, ζ_2)	$\omega = 40$	$\omega = 200$	$\omega = 40$	$\omega = 200$	$\omega = 40$	$\omega = 200$
2	AWC	(1, 1)	0.992	0.959	0.95	3.26	0.21	0.40
	VWC	(0, 1)	0.771	0.548	8.33	13.32	10.91	9.04
	HWC	(1, 0)	1.073	1.110	7.04	9.88	2.76	1.68
1	AWC	(1, 1)	0.995	0.967	0.96	3.26	0.22	0.44
	VWC	(0, 1)	0.821	0.592	9.22	13.41	9.99	8.76
	HWC	(1, 0)	1.169	1.341	8.62	10.55	6.76	3.55
0.5	AWC	(1, 1)	0.998	0.981	0.98	3.36	0.23	0.51
	VWC	(0, 1)	0.950	0.765	13.03	16.40	8.43	8.19
	HWC	(1, 0)	1.129	1.574	14.40	17.14	18.86	10.05

Finally, we provide in tables 1 and 2 the numerical values of some of our results, which can be used as benchmarks for numerical methods to be developed in the future to solve similar but more complicated problems. In these tables, we provide values for (i) the ratio of the flow rate with rotation to that without rotation, $Q/Q_{\rm nr}$, where $Q_{\rm nr}$ is given in (4.2), (ii) the ratio of the maximum magnitude of the transverse velocity to the maximum axial velocity, $|v|_{\max}/|u|_{\max}$, and (iii) the ratio of the mean magnitude of the secondary flow to the mean axial velocity, $\bar{v}_{\rm sf}/\bar{u}$, where $v_{\rm sf} = (v^2 + w^2)^{1/2}$ and the overbar denotes cross-sectional averaging. Speziale [18] remarked that the magnitude of the secondary flow should be of the order 1% of the axial flow to have a significant effect. Our values indicate that the secondary flow in the present problem can vary in the range of

$O(0.1-10)\%$ of the axial velocity, depending on b, ω, κ, ζ_1 and ζ_2. It is interesting to find that, in most cases of VWC and HWC, the ratio $|v|_{\max}/|u|_{\max}$ increases as ω increases. On the contrary, the corresponding ratio $\bar{v}_{\rm sf}/\bar{u}$ may decrease as ω increases. This is just to confirm what we have described above. A higher value of ω may strengthen the secondary flow locally, but will weaken the secondary flow field as a whole.

6. Concluding remarks

Motivated by the need to understand rotating electro-osmotic flow (EOF) with side wall effects, we have developed an analytical model for low-Rossby-number EOF through a rectangular microchannel rotating about an axis perpendicular to its own. The key findings are summarised as follows. First, we have examined in detail the flow structure of an Ekman–EDL layer, which is an Ekman layer modulated by electrokinetics, and is characterised by the Debye parameter normalized by the Ekman layer thickness. Outside this boundary layer is a geostrophic core, where the axial velocity decreases as the rotation speed increases according to the square root of the Ekman number. Second, when the channel is sufficiently wide or when all the walls are equally charged, the Coriolis force is always to decrease the mean flow and the effect is most appreciable when the Debye parameter is on the order of 10. In sharp contrast, in a channel of finite width, the Coriolis force may decrease or increase the mean flow, depending on the Debye parameter, if only the horizontal walls are charged. When the Debye parameter is very large (or the EDL is very thin), the flow rate is only modestly decreased by the channel rotation when all the walls are charged, but can be significantly increased by the rotation when only the horizontal walls are charged. Third, for flow in a square channel, we have shown axial velocity profiles to illustrate how geostrophic flow develops in the interior as the rotation speed increases. An order-of-magnitude analysis reveals that a Taylor–Proudman profile (i.e. the vanishing of the axial velocity gradient in the vertical direction) may materialise in the interior according to the square of the Ekman number. The development of the geostrophic core is accompanied by a rise or fall of the axial velocity in the core, depending on the electro-osmotic pumping near the walls. This explains why the flow rate may be increased or decreased by the rotation when only the horizontal walls or all the walls are charged. Fourth, we have also shown corresponding secondary flow fields to illustrate how different forms of circulatory cells may develop in the channel cross section. An increased favourable transverse pressure gradient near the centre is responsible for the generation of a counterclockwise vortex in the case when only the horizontal walls are charged. As the rotation speed increases, the secondary flow may be strengthened locally (owing to a stronger Ekman pumping near the walls), but can be weakened as a whole (owing to a weaker vorticity generation in the interior).

The present model can be readily extended to include an applied pressure gradient so as to examine combined pressure-driven and electro-osmotic flow through a rotating channel. It is also of practical interest to investigate the case in which the top and bottom walls have disparate zeta potentials, which may dramatically change the effect of rotation on the mean and secondary flows. Taking into account inertia effects, a numerical study is worth pursuing in the future to look into roll-cell instabilities arising from electro-osmotic flow in a rotating channel of a rectangular or circular cross section. Results can be compared with those reported in the literature for pressure-driven rotating channel flow.

Data accessibility. This article's data can be obtained from the authors.

Funding statement. The work was supported by the Research Grants Council of the Hong Kong Special Administrative Region, China, through Project No. HKU 715510E, and also by the University of Hong Kong through the Small Project Funding Scheme under Project Code 201309176109.

Author contributions. C.O.N. conceived and formulated the problem. The analysis was performed jointly by the two authors.

Conflict of interests. We have no competing interests.

References

1. Duffy DC, Gillis HL, Lin J, Sheppard Jr, NF, Kellogg GJ. 1999 Microfabricated centrifugal microfluidic systems: characterization and multiple enzymatic assays. *Anal. Chem.* **71**, 4669–4678.
2. Chang CC, Wang CY. 2011 Rotating electro-osmotic flow over a plate or between two plates. *Phys. Rev.* E **84**, 056320.
3. Xie ZY, Jian YJ. 2014 Rotating electroosmotic flow of power-law fluids at high zetapotentials. *Colloids Surf., A: Physicochem. Eng. Aspects* **461**, 231–239.
4. Li SX, Jian YJ, Xie ZY, Liu QS, Li FQ. 2015 Rotating electro-osmotic flow of third grade fluids between two microparallel plates. *Colloids Surf., A: Physicochem. Eng. Aspects* **470**, 240–247.
5. Gorkin R, Park J, Siegrist J, Amasia M, Lee BS, Park JM, Kim J, Kim H, Madouab M, Cho YK. 2010 Centrifugal microfluidics for biomedical applications. *Lab Chip* **10**, 1758–1773.
6. Wang GJ, Hsu WH, Chang YZ, Yang H. 2004 Centrifugal and electric field forces dual-pumping CD-like microfluidic platform for biomedical separation. *Biomed. Microdevices* **6**(1), 47–53.
7. Boettcher M, Jaeger M, Riegger L, Ducrée J, Zengerle R, Duschl C. 2006 Lab-on-chip-based cell separation by combining dielectrophoresis and centrifugation. *Biophys. Rev. Lett.* **1**, 443–451.
8. Martinez-Duarte R, Gorkin RA, Abi-Samrab K, Madou MJ. 2010 The integration of 3D carbon-electrode dielectrophoresis on a CD-like centrifugal microfluidic platform. *Lab Chip* **10**, 1030–1043.
9. Soong CY, Wang SH. 2004 Analysis of rotation-driven electrokinetic flow in microscale gap regions of rotating disk systems. *J. Colloid Interface Sci.* **269**, 484–498.
10. Takashima M. 1975 The effect of rotation on electrohydrodynamic instability. *Can. J. Phys.* **54**, 342-Ű347.
11. Othman MIA. 2004 Electrohydrodynamic instability of a rotating layer of a viscoelastic fluid heated from below. *Z. Angew. Math. Phys.* **55**, 468–482.
12. Ruo AC, Chang MH, Chen F. 2010 Effect of rotation on the electrohydrodynamic instability of a fluid layer with an electrical conductivity gradient. *Phys. Fluids* **22**, 024102.
13. Shivakumara IS, Akkanagamma M, Ng CO. 2013 Electrohydrodynamic instability of a rotating couple stress dielectric fluid layer. *Int. J. Heat Mass Trans.* **62**, 761–771.
14. Ducrée J, Haeberle S, Brenner T, Glatzel T, Zengerle R. 2006 Patterning of flow and mixing in rotating radial microchannels. *Microfluid. Nanofluid.* **2**, 97–105.
15. Greenspan HP. 1969 *Theory of rotating fluids*. Cambridge.
16. Pedlosky J. 1987 *Geophysical fluid dynamics*, 2nd edn. Springer.
17. Hart JE. 1971 Instability and secondary motion in a rotating channel flow. *J. Fluid Mech.* **45**, 341–351.
18. Speziale CG. 1982 Numerical study of viscous flow in rotating rectangular ducts *J. Fluid Mech.* **122**, 251–271.
19. Kheshgi HS, Scriven LE. 1985 Viscous flow through a rotating square channel. *Phys. Fluids* **28**(10), 2968–2979.
20. Nandakumar K, Raszillier H, Durst F. 1991 Flow through rotating rectangular ducts *Phys. Fluids A* **3**(5), 770–781.
21. Barua SN. 1954 Flow in a rotating straight pipe. *Proc. R. Soc. Lond.* A **227**, 133–139.